Theor. Comput. Fluid Dyn. (2017) 31:251–280
DOI 10.1007/s00162-017-0421-5

ORIGINAL ARTICLE

Nidhil M. A. Rehman · Anuj Kumar · Ratnesh K. Shukla

Influence of hydrodynamic slip on convective transport in flow past a circular cylinder

Received: 24 April 2016 / Accepted: 10 January 2017 / Published online: 1 February 2017

Abstract The presence of a finite tangential velocity on a hydrodynamically slipping surface is known to reduce vorticity production in bluff body flows substantially while at the same time enhancing its convection downstream and into the wake. Here, we investigate the effect of hydrodynamic slippage on the convective heat transfer (scalar transport) from a heated isothermal circular cylinder placed in a uniform cross-flow of an incompressible fluid through analytical and simulation techniques. At low Reynolds ($Re \ll 1$) and high Péclet ($Pe \gg 1$) numbers, our theoretical analysis based on Oseen and thermal boundary layer equations allows for an explicit determination of the dependence of the thermal transport on the non-dimensional slip length l_s. In this case, the surface-averaged Nusselt number, Nu transitions gradually between the asymptotic limits of $Nu \sim Pe^{1/3}$ and $Nu \sim Pe^{1/2}$ for no-slip ($l_s \to 0$) and shear-free ($l_s \to \infty$) boundaries, respectively. Boundary layer analysis also shows that the scaling $Nu \sim Pe^{1/2}$ holds for a shear-free cylinder surface in the asymptotic limit of $Re \gg 1$ so that the corresponding heat transfer rate becomes independent of the fluid viscosity. At finite Re, results from our two-dimensional simulations confirm the scaling $Nu \sim Pe^{1/2}$ for a shear-free boundary over the range $0.1 \leq Re \leq 10^3$ and $0.1 \leq Pr \leq 10$. A gradual transition from the lower asymptotic limit corresponding to a no-slip surface, to the upper limit for a shear-free boundary, with l_s, is observed in both the maximum slip velocity and the Nu. The local time-averaged Nusselt number Nu_θ for a shear-free surface exceeds the one for a no-slip surface all along the cylinder boundary except over the downstream portion where unsteady separation and flow reversal lead to an appreciable rise in the local heat transfer rates, especially at high Re and Pr. At a Reynolds number of 10^3, the formation of secondary recirculating eddy pairs results in appearance of additional local maxima in Nu_θ at locations that are in close proximity to the mean secondary stagnation points. As a consequence, Nu exhibits a non-monotonic variation with l_s increasing initially from its lowermost value for a no-slip surface and then decreasing before rising gradually toward the upper asymptotic limit for a shear-free cylinder. A non-monotonic dependence of the spanwise-averaged Nu on l_s is observed in three dimensions as well with the three-dimensional wake instabilities that appear at sufficiently low l_s, strongly influencing the convective thermal transport from the cylinder. The analogy between heat transfer and single-component mass transfer implies that our results can directly be applied to determine the dependency of convective mass transfer of a single solute on hydrodynamic slip length in similar configurations through straightforward replacement of Nu and Pr with Sherwood and Schmidt numbers, respectively.

Keywords Bluff body flows · Convective transport · Hydrodynamic slip

Communicated by Sergio Pirozzoli.

Nidhil M. A. Rehman · A. Kumar · R. K. Shukla (✉)
Department of Mechanical Engineering, Indian Institute of Science, Bangalore 560012, India
E-mail: ratnesh@mecheng.iisc.ernet.in
Tel.: +91-80-2293-3234

1 Introduction

Introduction of a finite slip at the fluid-solid boundary, in typical bluff body flows, is known to reduce vorticity production while at the same time enhancing its convection downstream [1]. The reduction in vorticity production is most pronounced in the case of a shear-free (perfect slip) boundary for which the surface vorticity depends only weakly on Reynolds number and in the asymptotic limit of infinite Reynolds number, becomes directly and inversely proportional to the local tangential surface velocity and the radius of curvature, respectively. The suppression of vorticity, combined with its increasingly efficient convection, owing to a pronounced increase in the tangential surface velocity with rising slip length, results in a substantial reduction in the flow separation and unsteadiness and also the hydrodynamic loads [2–5]. The possibility of achieving relatively large reductions in the drag force through sustained hydrodynamic slip has been the principal motivation behind the recent interest in the development of engineered superhydrophobic surfaces [6,7]. In the past, slip lengths ranging from 20 to nearly 200 μm have been realized through textured superhydrophobic surfaces [6].

In general, the finite tangential surface velocity that reduces the wall-normal velocity gradients and therefore the vorticity generation at a hydrodynamically slipping boundary is expected to enable efficient convection of heat or mass from it. Indeed increasing slip augments transport coefficients substantially even in the low Reynolds number regime in which the hydrodynamic slip-induced enhancement in the convective flow velocity is expected to remain minimal. Thus, for $Re \to 0$ and $Pe \gg 1$, the transport coefficients for uniform flow past a shear-free boundary are known to exhibit a power law scaling of $Pe^{1/2}$ that differs remarkably from the scaling law of $Pe^{1/3}$ for uniform flow past a no-slip surface [8]. Similar scaling exponents of $1/3$ and $1/2$ for the local Nusselt number corresponding to no-slip and shear-free boundaries, respectively, were obtained for the Graetz-Nusselt thermal entry length problem concerning growth of thermal boundary layer in a laminar fully developed slip-dependent velocity profile, in the recent work of Hasse et al. [9]. Furthermore, with rising slip the local and developed Nusselt numbers were found to gradually transition between the two distinct limits for no-slip and shear-free boundaries [9].

In both the creeping and the hydrodynamically full-developed laminar flow conditions considered in the previous works cited above, flow separation or reversal is not encountered and the flow field remains free of recirculating regions. In both these scenarios, an increase in the convective flow speed enabled by the rising slip length is expected to lead to a monotonic increase in the convective transport coefficients. In finite Re bluff body flows, however, the situation becomes complicated due to the emergence of recirculating wakes. At finite-Re, separation and unsteady vortex shedding over non-planar no-slip boundaries lead to formation of vortical velocity fields which promote transverse fluid mixing and augment convective transport through a reduction in thermal boundary layer thickness. Introduction of slip over such surfaces results in a reduction, and, for sufficiently large slip lengths, complete elimination of flow separation and vortex shedding. The reduction in the intensity or complete absence of recirculating regions allows the thermal boundary layer to grow over the downstream portion of the boundary and therefore limits the local convective transport from it. Thus, to a large extent, the potential gain in the convective transport over the upstream portion of a hydrodynamically slipping bluff body is offset by the loss over the downstream portion owing to the suppression of recirculating wakes. The relative dominance of these two competing effects should determine whether or not an overall increase in the convective transport is achieved in bluff body flows with finite slip. Thus, unlike the case of planar surfaces, it is not immediately clear whether or not application of hydrodynamic slip in bluff body flows results in increased global convective heat or mass transfer at some pre-specified Reynolds and Prandtl numbers. Given the existence of hydrodynamic slip over a wide range of continuum flows involving singular corners [10–12], moving contact lines [13,14] and hydrophobic surfaces [15,16] (also see [6,17]), an investigation into the anticipated non-trivial dependence of the convective transport coefficients on hydrodynamic slip is of prime importance. An understanding of this dependence at low and moderate Reynolds numbers can aid in the design of configurations that overcome the challenge of achieving large convective transport in miniaturized flow systems. Additionally, given the direct analogy between heat transfer and single-component mass transfer, hydrodynamic slip-induced enhancement in the local convective transport rates could be usefully employed in relevant technological and biological systems to maximize chemical adsorption or nutrient uptake.

In this work, we investigate the competing roles of the hydrodynamic slip in increasing and decreasing convective heat transport from the upstream and downstream portions of a hydrodynamically slipping cylindrical surface. As in the case of creeping or fully developed pipe flow configurations, with increasing slip length or equivalently the tangential surface velocity we find a monotonic increase in the surface-averaged convective transport coefficients for $Re \ll 1$ and $Pe \gg 1$. Moreover, in the absence of recirculating wakes in the low Re regime, we observe a monotonic increase in the thermal boundary layer thickness and a corresponding

monotonic decline in the local convective transport from the forward to the rear stagnation point along the hydrodynamically slipping cylinder boundary. Both local and average (time- and surface-averaged) convective transport coefficients are strongly influenced by the appearance of primary and secondary vortical structures and unsteady vortex shedding at finite Re. In particular, with the introduction of a relatively small slip, we observe a remarkably sharp rise in the time-averaged local Nusselt number close to the rear stagnation point. Upon further increase in slip length, this sharp rise in Nu disappears gradually as the primary recirculation region in the wake of the circular cylinder is largely suppressed. The sharp initial rise of the local Nu with slip length is especially pronounced at higher Re. At a Reynolds number of 10^3, this local rise is large enough to effect a change in the otherwise monotonic variation of the average Nusselt number with slip length.

Apart from continuum flows of dense fluids, hydrodynamic slip is routinely encountered in rarefied gas flows over solid surfaces [6,18]. In rarefied flows, the hydrodynamic slip that results in a jump in tangential velocity at the solid-fluid interface is accompanied by a jump in the surface temperature as well. Maxwell's velocity slip and Smoluchowski's temperature jump conditions enable the thermal and tangential velocity discontinuities to be incorporated as first- or higher-order (in Knudsen number) temperature and velocity boundary conditions within the continuum framework for rarefied flows [18–21]. Utilizing such an approach, the effect of hydrodynamic and thermal slips on the flow characteristics and the temperature field has been investigated for flow past both planar and cylindrical geometries theoretically [22–24] and through computations [25–27]. In [26], steady calculations based on stream-function vorticity formulation showed that an increase in the Knudsen number Kn from 0 to 0.05 at a fixed $Re = 40$ led to a rise in the tangential surface velocity and a decline in the drag coefficient, in accordance with the work of Legendre et al. [2]. Furthermore, the loss in the convective transport, owing to the existence of a finite temperature jump at the surface, was found to overwhelm the gain enabled by the rising tangential surface velocity. Therefore, a net reduction in the Nusselt number was observed with Kn at $Re = 10$, 20 and 40, over the range $Kn \leq 0.05$.

A key distinction between these previous works and the present investigation lies in our focus on continuum flows of dense fluids with hydrodynamic slip as opposed to rarefied slip flows. As in the case of rarified flows, the presence of a finite tangential surface velocity must be accounted for in the physical model employed for describing dense fluid continuum flows with finite hydrodynamic slip. However, in stark contrast to rarefied slip flows for which the effective slip length and therefore the maximum tangential surface velocity are both limited by the Knudsen number range $0.01 \leq Kn \leq 0.1$ [18], no restrictions on the slip length can generally be placed in dense fluid continuum flows (slip length becomes unbounded for a shear-free boundary). Thus, significantly larger slip velocities and convective transport rates can in principle be achieved. Moreover, unlike the case of rarefied flows, the jump in the surface temperature is negligible so that it suffices to directly impose the requisite isothermal or flux condition at the solid boundary [18,19]. Therefore, following previous works on dense fluid continuum flows with finite slip [2–5,9,11,14] we rely on the Navier slip condition to account for the hydrodynamic slip on the cylinder surface. To fully characterize the effect of hydrodynamic slip on convective transport, we span a relatively wide range of Reynolds and Prandtl numbers for slip lengths ranging from zero for a no-slip boundary, to infinity for a shear-free surface. To the best of our knowledge, an exhaustive investigation aimed at establishing the dependence of Nu on Re, Pr and non-dimensional slip length, through an analysis of the competing roles of hydrodynamic slip in increasing and decreasing the convective transport from the upstream and downstream portions of the cylinder boundary, respectively, has not appeared in the literature till now.

This paper is organized as follows: the setup of the flow configuration including governing equations and hydrodynamic slip boundary condition is described in Sect. 2. Results from a boundary layer analysis at large Péclet numbers establishing the completely analogous relationships between the non-dimensional slip length and the Nusselt number, and the maximum slip velocity, under creeping-flow condition, are presented in Sect. 3. The details of numerical discretization methodology employed for simulation-based investigations at finite Re are presented in Sect. 4. Results from the simulations characterizing the influence of hydrodynamic slip on both local and average Nusselt numbers over the range $0.1 \leq Re \leq 10^3$ and $0.1 \leq Pr \leq 10$ are presented and analyzed in Sect. 5. Section 6 summarizes the principal conclusions and outlines directions for future investigations.

2 Problem formulation

We consider a two-dimensional configuration consisting of uniform flow of a viscous incompressible fluid past a heated circular cylinder of diameter D. The temperature T_s at the surface of the isothermal circular cylinder

exceeds the far-field temperature T_∞ in the surrounding fluid. The governing incompressible Navier–Stokes equations for this setup are given by

$$\frac{\partial \mathbf{u}}{\partial t} + \mathbf{u} \cdot \nabla \mathbf{u} = -\frac{1}{\rho} \nabla p + \nu \nabla^2 \mathbf{u}, \quad \nabla \cdot \mathbf{u} = 0, \tag{1}$$

where t denotes the time, $\mathbf{u} = (u_r, u_\theta)$ is the velocity field in cylindrical polar coordinates with p as the pressure and ρ and ν as the density and the kinematic viscosity of the incompressible fluid, respectively. The Reynolds number based on the diameter of the cylinder is $Re = U_\infty D/\nu$ with $U_\infty \mathbf{i}$ as the far-field uniform velocity along the positive $x-$ direction $\mathbf{i}$. The no-through-flow and the Navier slip boundary conditions [28] on the surface of the cylinder are given by

$$u_r(a, \theta) = 0, \quad \text{and} \quad \left.\frac{\partial u_\theta}{\partial r}\right|_{r=a} = \frac{u_\theta(a, \theta)}{a} \left(1 + \frac{1}{l_s}\right), \tag{2}$$

respectively, where l_s denotes the non-dimensional slip length and $a = D/2$ is the radius of the circular cylinder.

The normalized temperature $\Theta = (T - T_\infty) / (T_s - T_\infty)$ is given by the unsteady convection–diffusion equation

$$\frac{\partial \Theta}{\partial t} + \mathbf{u} \cdot \nabla \Theta = \alpha \nabla^2 \Theta, \tag{3}$$

where α denotes the thermal diffusivity. In writing Eqs. (1), (2) and (3), we have assumed that within the range of temperature variations, fluid and surface properties ρ, ν, l_s and α undergo minimal changes and can therefore be treated as constants. Furthermore, the heat generation term arising out of frictional heating from viscous dissipation has been ignored (Eckert number $Ec \ll 1$). The Péclet number $Pe = RePr$ with $Pr = \nu/\alpha$ as the Prandtl number. The normalized temperature Θ satisfies the isothermal boundary condition $\Theta = 1$ imposed at the cylinder surface $r = a$ and the far-field condition $\Theta \to 0$ as $r \to \infty$. The rate of heat transfer from the surface of the circular cylinder is quantified through the local Nusselt number

$$Nu_\theta = -D \widehat{\left(\frac{\partial \Theta}{\partial r}\right)}\Bigg|_{r=a}, \tag{4}$$

where a hat has been used to denote time-averaged normalized temperature gradient. The average Nusselt number is related to the local Nusselt number through

$$Nu = \frac{1}{2\pi} \int_0^{2\pi} Nu_\theta\,(\theta)\ \mathrm{d}\theta. \tag{5}$$

In the following sections, we aim to establish the dependence of both Nu and Nu_θ on the non-dimensional parameters l_s, Pr and Re first through a boundary layer analysis for large Péclet numbers and subsequently through simulations.

3 Boundary layer analysis

In the asymptotic limit of $Re \ll 1$, the general solution of Oseen's equations in polar cylindrical coordinates [29, 30] can be used to determine the velocity and pressure fields for a prescribed tangential surface velocity profile [31]. Furthermore, in the limiting case of $Re \gg 1$ and $l_s \to \infty$, the boundary layer over a shear-free cylinder does not separate and perturbations to the inviscid potential flow field remain $\mathrm{O}(Re^{-1/2})$ [31] (also see [32,33]). Therefore, to a leading order in Re, the velocity and pressure fields for flow past a shear-free circular cylinder are given by the inviscid potential flow.

In both the limiting cases described above, the availability of explicit expressions for the velocity field allows us to quantify the effect of slip on convective thermal transport for $Pe \gg 1$. In the following subsections, we establish the dependence of Nu on Pe through an analysis of thermal boundary layer equations for $Pe \gg 1$, given the velocity fields for creeping flow and high Reynolds number flow past a shear-free cylinder surface.

3.1 $Re \ll 1$ and $Pe \gg 1$

General relationships that express the dependence of the velocity field on prescribed non-dimensional slip length l_s in the asymptotic limit of $Re \ll 1$ can be deduced from the solution of Oseen's equations (see "Appendix 1"). Substitution of the radial and circumferential velocity components into Eq. (3) yields an equation for the normalized temperature distribution. In the asymptotic limit of $Pe \gg 1$, the thermal gradients in the boundary layer along the wall-normal direction exceed those along the streamwise direction significantly [34]. In the region within the boundary layer, the radial and tangential components of the velocity vector can be expressed as

$$\begin{aligned} u_r(r,\theta) &= U_\infty \cos\theta \left\{\alpha y + \beta y^2 + \mathrm{O}(y^3)\right\}, \\ u_\theta(r,\theta) &= U_\infty \sin\theta \left\{-\alpha + 2\beta\left(\frac{l_s+1}{l_s-1}\right) y + \mathrm{O}(y^2)\right\}, \end{aligned} \tag{6}$$

where the rescaled coordinate is $r = a(1+y)$ and

$$\alpha = \frac{4l_s}{1-2\gamma-2\ln(Re/8)+4l_s\left[1-\gamma-\ln(Re/8)\right]} \quad \text{and} \quad \beta = \alpha\left(\frac{1-l_s}{2l_s}\right). \tag{7}$$

In the rescaled coordinate system, the thermal boundary layer equation then assumes the following form

$$\cos\theta\left\{\alpha y + \beta y^2\right\}\frac{\partial\Theta}{\partial y} + \left(-\alpha + 2\beta\frac{1}{l_s-1}y\right)\sin\theta\frac{\partial\Theta}{\partial\theta} = \frac{2}{Pe}\frac{\partial^2\Theta}{\partial y^2}. \tag{8}$$

Note that over the entire range of non-dimensional slip length $0 \le l_s \le \infty$, coefficients α and β do not vanish simultaneously so that it suffices to retain just the first two terms in the expansion of radial and tangential velocity components given by Eq. (8).

In case of a hydrodynamically slipping cylinder surface with non-vanishing $\alpha \sim \mathrm{O}(1)$, the first term in Eq. (6) for the expansion of the radial and tangential velocity components dominates the others. Retaining only this dominant term in the thermal boundary layer Eq. (8), it can be shown that the transformation

$$Y = \sqrt{\alpha Pe/2}\, y \sin\theta, \quad X = 1 + \cos\theta, \tag{9}$$

reduces Eq. (8) to $\Theta_X = \Theta_{YY}$, for which the similarity solution that satisfies the boundary conditions $\Theta(Y=0,X) = 1$ and $\Theta(Y\to\infty,X) = 0$ is given by $\Theta(\eta) = \mathrm{erfc}(\eta)$, where $\eta = Y/(2\sqrt{X})$. The similarity solution can be used to derive the following expressions for the local and average Nusselt numbers:

$$Nu_\theta^{PS} = \sqrt{\frac{4\alpha Pe}{\pi}}\sin\left(\frac{\theta}{2}\right) \quad \Longrightarrow \quad Nu^{PS} = 0.718\,(\alpha Pe)^{1/2}, \tag{10}$$

where the superscript PS denotes partial slip.

Thus, for a partially slipping cylindrical surface with $\alpha \sim \mathrm{O}(1)$ we obtain the scaling law $Nu \sim Pe^{1/2}$ that is expected to hold for convective transport from a shear-free boundary [8]. It is worth noting that the thermal boundary layer analysis wrongly predicts that the local Nusselt number vanishes, while the thermal boundary layer thickness $\delta_{BL}^{\Theta} \sim \mathrm{cosec}\,(\theta/2)$ diverges at the rear stagnation point ($\theta = 0$). This unphysical behavior is indicative of a breakdown of the assumption of radial thermal gradient being significantly larger than the circumferential temperature gradient in the boundary layer region. Close to the rear stagnation region, the convective terms are balanced by both the radial and circumferential diffusive terms, each of which are of the same order and therefore cannot be neglected in comparison with the other.

Equation (10) holds only for a cylindrical surface with relatively large hydrodynamic slip ($\alpha \sim \mathrm{O}(1)$). In the limiting case of $\alpha \to 0$, the first term in the asymptotic expansions of the velocity field given by Eq. (6) is vanishingly small. Thus, to a leading order, the radial and tangential velocity components exhibit a quadratic and linear dependence on the rescaled wall-normal coordinate y, respectively. It can be shown that application of the following transformation

$$Y = (\lambda Pe/2)^{1/3}\, y\sqrt{\sin\theta}, \quad X = \int_\theta^\pi \sqrt{\sin t}\,\mathrm{d}t, \quad \text{where} \quad \lambda = \frac{4}{1-2\gamma-2\ln(Re/8)}, \tag{11}$$

converts the thermal boundary layer Eq. (8) for a no-slip cylindrical surface with $\alpha = 0$ (or equivalently, $l_s = 0$) to

$$Y\frac{\partial \Theta}{\partial X} = \frac{\partial^2 \Theta}{\partial Y^2}. \tag{12}$$

Equation (12) admits the following similarity solution

$$\Theta = \left[\left(\int_0^\infty \exp\left(\frac{-t^3}{9}\right) \mathrm{d}t\right)\right]^{-1} \left(\int_\eta^\infty \exp\left(\frac{-t^3}{9}\right) \mathrm{d}t\right), \quad \text{with } \eta = \frac{Y}{X^{1/3}}, \tag{13}$$

which also satisfies the boundary conditions $\Theta\,(Y = 0, X) = 1$ and $\Theta\,(Y \to \infty, X) \to 0$. Corresponding local and average Nusselt numbers are given by

$$Nu_\theta^{NS} = \frac{2\,(3\lambda Pe/2)^{1/3}}{\Gamma(1/3)} \left(\frac{\sqrt{\sin\theta}}{\left[\int_\theta^\pi \sqrt{\sin t}\,\mathrm{d}t\right]^{1/3}}\right) \quad \text{and} \quad Nu^{NS} = 0.73\,(\lambda Pe)^{1/3}, \tag{14}$$

where the superscript NS denotes no-slip. Above expressions are consistent with the scaling law $Nu \sim Pe^{1/3}$ that holds for convective transport from a two-dimensional body with no-slip boundary under uniform creeping-flow conditions.

For intermediate slip lengths corresponding to a cylindrical surface with partial slip, the Nusselt number is expected to lie in between the two asymptotic limits given by Eqs. (14) and (10). As l_s increases from 0 to ∞, the Nusselt number is expected to transition gradually from its lower asymptotic limit for a no-slip boundary to the upper asymptotic limit for a shear-free surface. The nature of this transition and the dependence of the Nusselt number on l_s can be established through a general solution of Eq. (8) that takes into account both the first- and second-order terms in the asymptotic expansion given by Eq. (6). Unfortunately, determination of such a general explicit analytical solution to this seemingly difficult problem has not been possible. Nevertheless, the expression Eq. (10) for the Nusselt number corresponding to flow past a circular cylinder with partial slip can be used to deduce useful information regarding this transition. For $\alpha \sim Pe^{-1/3}$ or equivalently $l_s \sim Pe^{-1/3}$, we find $Nu^{NS} \sim Pe^{1/3} \sim Nu^{PS}$. The Nusselt number Nu can therefore be expected to reach a value close to the lower asymptotic limit given by Eq. (14) for a no-slip cylinder surface. This hypothesis can be rigorously established by deriving an explicit expression for the Nusselt number with full consideration of both the linear and quadratic terms in the expansion of u_r and u_θ. As shown in "Appendix 2," the final outcome of such an analysis that relies on series expansion in increasing powers of $Pe^{1/3}$, is the following expression for the Nusselt number:

$$Nu = (\lambda Pe)^{1/3}\left(0.73 + C_1\frac{\alpha Pe^{1/3}}{\lambda^{2/3}} + C_2\left\{\frac{\alpha Pe^{1/3}}{\lambda^{2/3}}\right\}^2 + \cdots\right), \quad \text{for} \quad \alpha Pe^{1/3} < \mathrm{O}\left(\lambda^{2/3}\right), \tag{15}$$

where C_1 and C_2 are constants. For relatively small slip lengths $l_s \sim Pe^{-n}$ with $0 < n < 1/6$, $\alpha \sim l_s$, so that the Nusselt number $Nu \sim Pe^{(1-n)/2}$. For $l_s \sim \mathrm{O}(1)$ and $l_s \gg 1$, $\alpha \sim \mathrm{O}(1)$, so that $Nu \sim Pe^{1/2}$. Thus, beyond $l_s \gtrapprox 1$ the Nusselt number asymptotes toward the upper limit for a shear-free cylinder surface.

Given the striking difference in the Nusselt number scaling exponents for the shear-free and no-slip surfaces, one would expect the local Nusselt number for a shear-free boundary to significantly exceed the one for a no-slip surface. A careful examination of Eqs. (10) and (14) reveals that $Nu_\theta^{PS}(l_s \to \infty) > Nu_\theta^{NS}$ over majority of the cylinder surface except in the vicinity of the rear stagnation region. Thus, we find that for $\theta \lessapprox 1.28\lambda^{2/3}Pe^{-1/3}/\alpha(l_s \to \infty)$, the local Nusselt number for a no-slip cylinder surface exceeds the one for a shear-free cylinder. Clearly, the region over which $Nu_\theta^{NS} > Nu_\theta^{PS}(l_s \to \infty)$ shrinks with increasing Péclet number.

It may seem that in the absence of flow separation and recirculating wakes at vanishing Reynolds numbers, the decrease in local Nusselt number with increasing slip, as predicted from the thermal boundary layer analysis, is a spurious artifact that is a direct consequence of an inappropriate neglect of the circumferential temperature gradient in the vicinity of the rear stagnation point. To conclusively establish whether or not $Nu_\theta^{PS}(l_s \to \infty) > Nu_\theta^{NS}$ close to the rear stagnation point or elsewhere on the cylinder surface, we consider solving Eq. (3) without invoking boundary layer assumptions. Using high-order discretization methods described later in Sect. 4, we compute approximate solution of Eq. (3) with the flow velocities prescribed through Eq. (29).

Figure 1 depicts the local Nusselt number Nu_θ for Reynolds numbers 10^{-3} and 10^{-2} over a range of slip lengths and Péclet numbers. In accordance with the theoretical prediction from the thermal boundary layer analysis, we find that the local Nusselt number rises with increasing slip length at the forward stagnation point ($\theta = \pi$) and over a major portion of the cylinder surface. More importantly, a reversal of this trend is observed in the vicinity of the rear stagnation point so that the local Nusselt number is the least for a shear-free boundary and the highest for a no-slip surface in this region. Note that this observation too is consistent with the theoretical prediction from the boundary layer analysis even though the theoretical estimate of the local Nusselt number in the rear stagnation region is certainly erroneous [for instance $Nu_\theta\,(\theta = 0) = 0$ from the boundary layer solutions given by Eqs. (10) and (14)].

With rising slip length, the surface-averaged Nusselt number undergoes a gradual transition from its asymptotic lower limit for a no-slip surface to the upper limit for a shear-free cylindrical surface. This transition is clearly evidenced from the top frames of Fig. 2 that depict Nu as a function of Pe for $Re = 10^{-3}$ and 10^{-2} over a range of slip lengths. The exponent in the power law scaling of Nu with Pe also transitions from $1/3$ to $1/2$ as l_s varies from 0 to ∞.

To illustrate the transition in Nusselt number more effectively, we present the dependence of normalized Nusselt number, defined as

$$Nu_{\text{Norm}}\,(l_s) = \frac{Nu\,(l_s) - Nu\,(0)}{Nu\,(\infty) - Nu\,(0)}, \tag{16}$$

on the slip length l_s in the bottom frames of Fig. 2. For both $Re = 10^{-3}$ and 10^{-2}, we find a remarkable collapse of Nu_{Norm} for various Pe. Thus, the dependence of Nu on Pe is effectively captured through the normalization given by Eq. (16). Figure 2 also depicts a comparison of the discrete data points obtained from the simulations with an expression obtained by replacing the normalized maximum slip velocity in Eq. (30) with the normalized Nusselt number. The excellent agreement between the continuous curve and the discrete points from the simulations implies that in the low-Re regime the normalized Nusselt number is given by the following expression analogous to Eq. (30):

$$Nu_{\text{Norm}}\,(l_s) = \frac{l_s}{l_s + C(Re)}, \tag{17}$$

where $C(Re)$ is given by Eq. (31). Thus, in the asymptotic limit of $Re \to 0$, an increase in the maximum normalized slip velocity translates to a proportionate increase in the corresponding Nusselt number for $Pe \gg 1$.

3.2 $Re \gg 1, l_s \to \infty$ and $Pe \gg 1$

In the asymptotic limit of $Re \to \infty$ and $Pe \to \infty$, an analysis of the thermal boundary layer equation can be used to determine the Nusselt number for convective thermal transport from a shear-free cylinder. For $Re \gg 1$ and $l_s \to \infty$, corresponding to a shear-free cylinder surface, to a leading order in Re, the velocity field is given by the potential flow solution. An asymptotic expansion of the velocity field then shows that the radial and tangential velocity components are given by Eq. (6) with $\alpha = 2$. Then, proceeding with the analysis outlined in the previous section we obtain $Nu^{SF} = 1.016 Pe^{1/2}$, where the superscript SF denotes shear-free cylinder surface.

3.3 $Pe \ll 1$

The expansion techniques employed above can also be used to determine the local and average Nusselt numbers in the asymptotic limit $Pe \ll 1$. In this case, the thermal boundary layer is significantly larger than the hydrodynamic boundary layer so that the velocity components in Eq. (6) can be taken from the potential flow solution ($\alpha = 2$), as in the previous subsection. Furthermore, using matched asymptotic expansions the following expression for the temperature field can be obtained

$$\Theta(r, \theta) = 1 - \frac{\ln\,(r/a)}{\ln\,(8/Pe) - \gamma} + \mathrm{O}\,(Pe)\,, \tag{18}$$

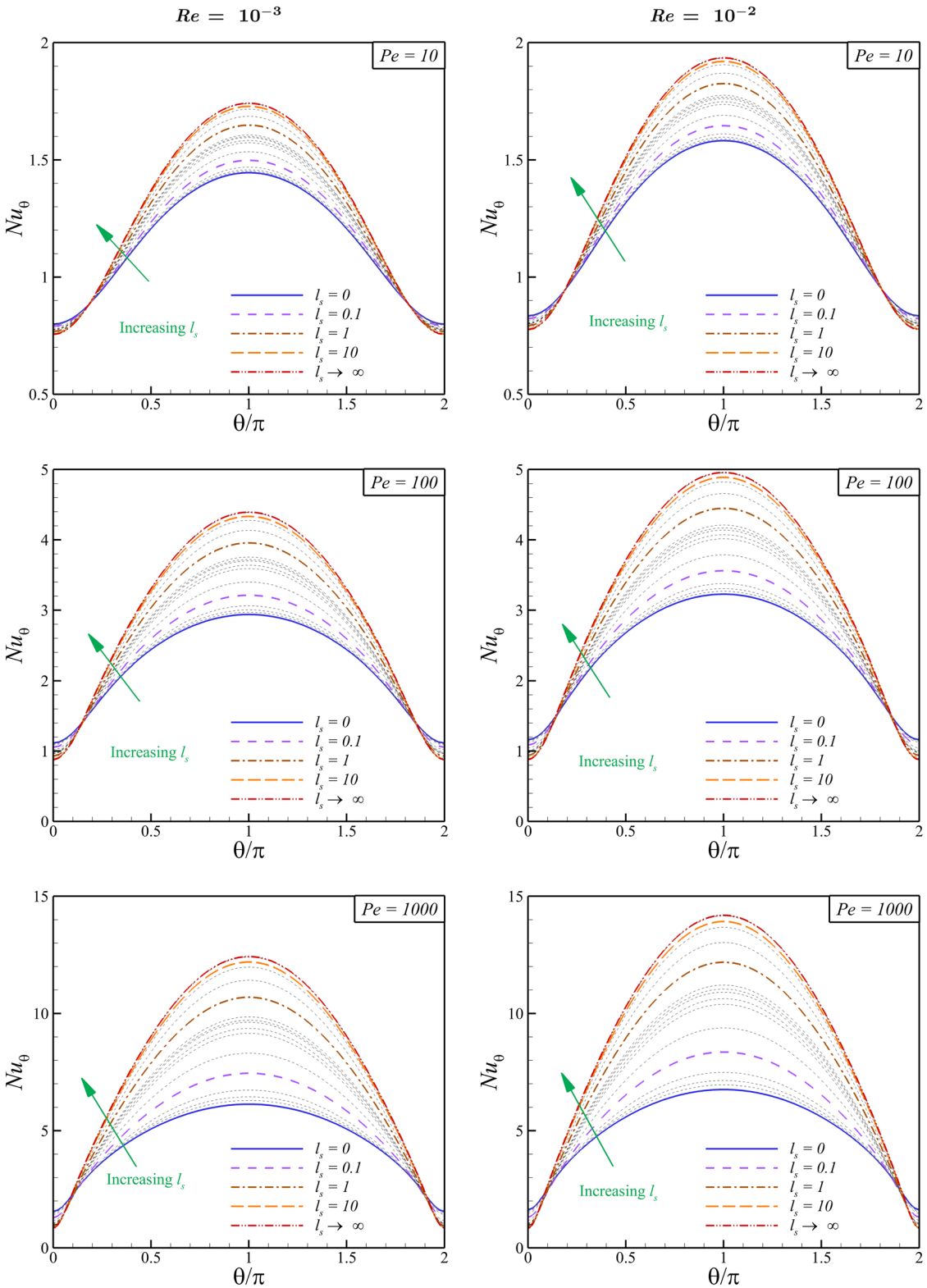

Fig. 1 Nusselt number Nu_θ along the cylinder surface for (*left*) $Re = 10^{-3}$ and (*right*) $Re = 10^{-2}$

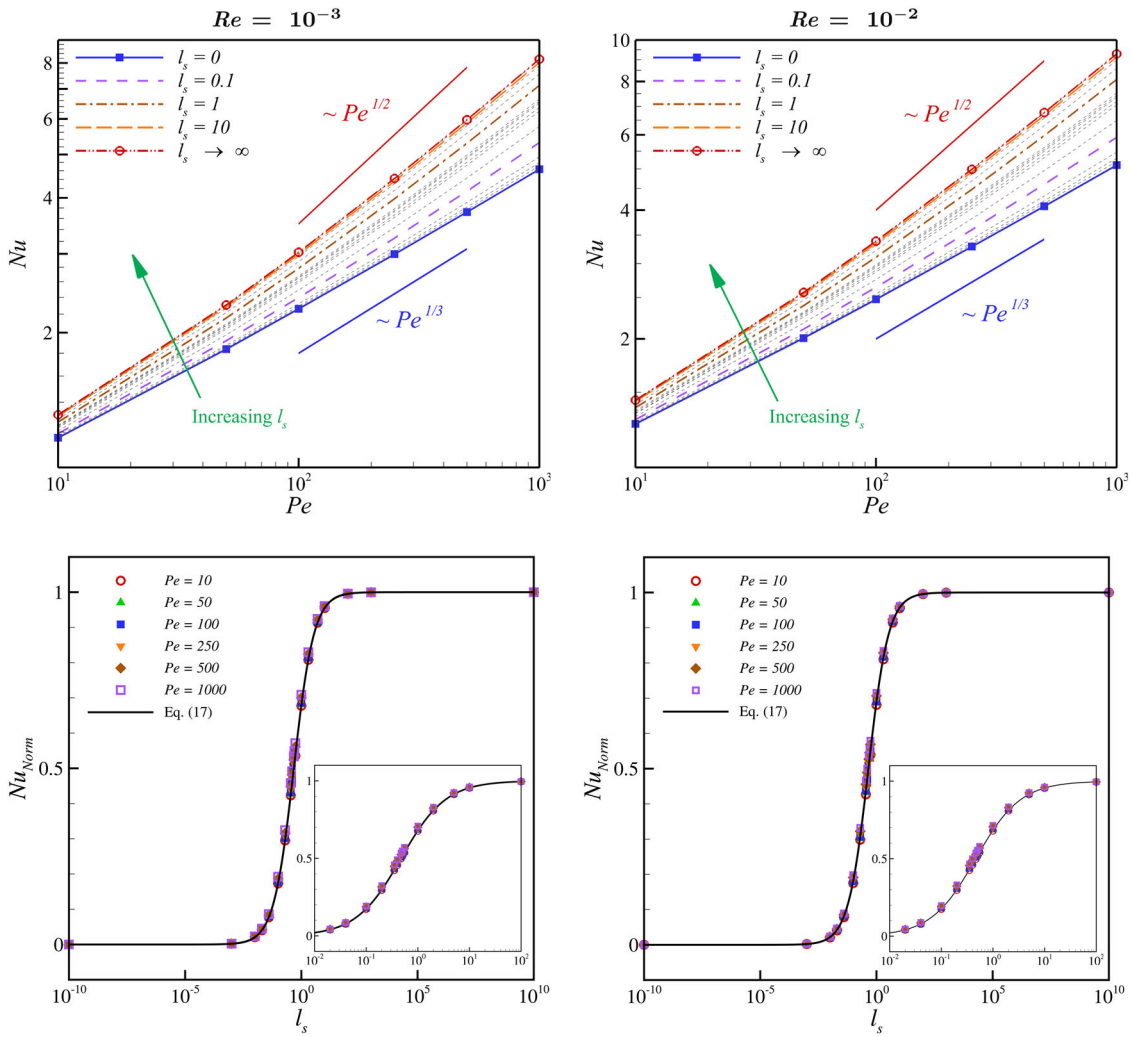

Fig. 2 (*Top*) Surface-averaged Nusselt number (Nu) as a function of Pe for (*left*) $Re = 10^{-3}$ and (*right*) $Re = 10^{-2}$. (*Bottom*) Normalized Nusselt number Nu_{Norm} as a function of l_s for (*left*) $Re = 10^{-3}$ and (*right*) $Re = 10^{-2}$

from which we deduce

$$Nu = \frac{2}{\ln(8/Pe) - \gamma} + \mathrm{O}\left(Pe^2\right), \tag{19}$$

in agreement with [22,23]. The dominance of conduction over convection at $Pe \ll 1$ implies that to a leading order, the temperature distribution is radially symmetric, with the asymmetric θ-dependent terms featuring only in the next higher-order expressions (w.r.t. Pe) in the matched asymptotic expansion.

4 Simulation details

Next, we consider establishing the dependence of Nu on l_s and Pr at moderate and high Reynolds numbers. In the absence of analytical solutions for flow past a circular cylinder with partial slippage, we solve Eqs. (1) and (3) numerically. We consider high-order spatial discretization of the primitive variable formulation of the incompressible Navier–Stokes equations in polar cylindrical coordinates using 10th-order non-uniform mesh compact schemes [35,36] along the radial direction and a Fourier spectral method along the periodic circumferential direction. For time advancement, we utilize the second-order accurate projection method of Hugues and Randriamampianina [37] that relies on a semi-implicit Adams Bashforth and Backward Differentiation

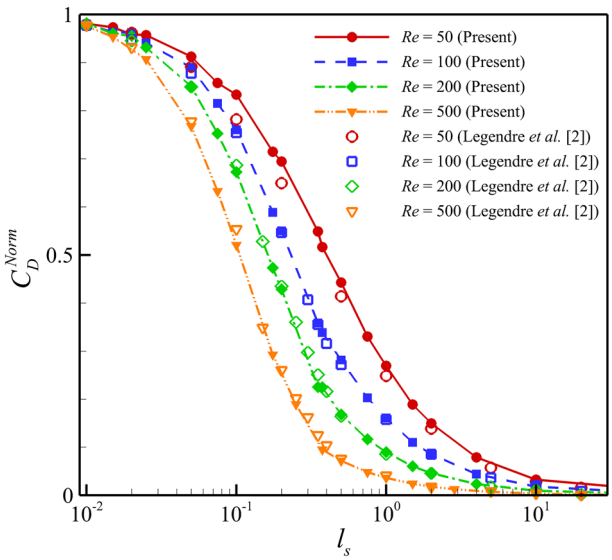

Fig. 3 Normalized drag coefficient C_D^{Norm} as a function of l_s at $Re = 50$, 100, 200 and 500 compared with the results of Legendre et al. [2]

formula (AB/BDI2) for temporal discretization of the nonlinear convective and linear viscous terms, respectively. Additional details of the discretization methodology including validation tests for flow past circular and elliptic cylinders with prescribed no-slip and shear-free boundary conditions can be found in previous works [31,38]. For spatiotemporal discretization of the advection–diffusion equation (3) for non-dimensional temperature Θ, we perform a straightforward extension of the discretization technique adopted for approximating the momentum equation. To further verify our simulation methodology for flow past a circular cylinder with partial slip, we compare the normalized drag coefficients computed from our simulations with the results reported in [2]. This comparison depicted in Fig. 3 shows our results to be in reasonably good agreement with the ones presented in [2]. This attests the accuracy of our discretization methodology for intermediate slip lengths that lie in between the two asymptotic limits of zero and infinite l_s corresponding to no-slip and shear-free cylinder boundaries, respectively.

5 Simulation results

To investigate the effect of slip on temperature distribution and the local and average Nusselt numbers, we perform simulations for varying slip lengths over a range of Reynolds ($Re = 0.1$, 1, 5, 10, 20, 50, 100, 200, 300, 500 and 1000) and Prandtl numbers ($Pr = 0.1, 0.25, 0.5, 1, 2, 5$ and 10). In all our simulations, we ensured convergence with respect to the discretization parameters through successive refinements in both mesh spacing and time step size.

To begin with, we illustrate the effect of hydrodynamic slip on flow field and temperature distribution at various Reynolds numbers for a fixed Prandtl number of 1. Left frames of Fig. 4 depict the vorticity and streamlines for varying l_s at $Re = 1$. The corresponding temperature field is depicted in the right frames of Fig. 4. With increasing slip length, a slight decrease in the vorticity levels is clearly evidenced from the left frames of Fig. 4. The corresponding temperature field seems relatively unaffected by an increase in the slip length and thus no noticeable change in the temperature distribution is observed with varying l_s (right frames of Fig. 4). At a Péclet number of 1, the contribution from diffusive thermal transport is expected to be as important as the contribution from convective transport. Hence, the temperature field remains almost insensitive to an increase in the convective speed enabled by rising l_s.

At a higher Reynolds number of 10, an increase in the hydrodynamic slip at the cylinder surface results in a more prominent reduction in the vorticity, as evidenced from the left frames of Fig. 5. Compared to the previous $Re = 1$ case, the thermal boundary layers are thinner (see right frames of Fig. 5) as the corresponding Péclet number is an order of magnitude higher ($Pe = 10$). Furthermore, with increasing slip, in the upstream region of the flow domain, the transition in the non-dimensional temperature, from a maximum of $\Theta = 1$ at the

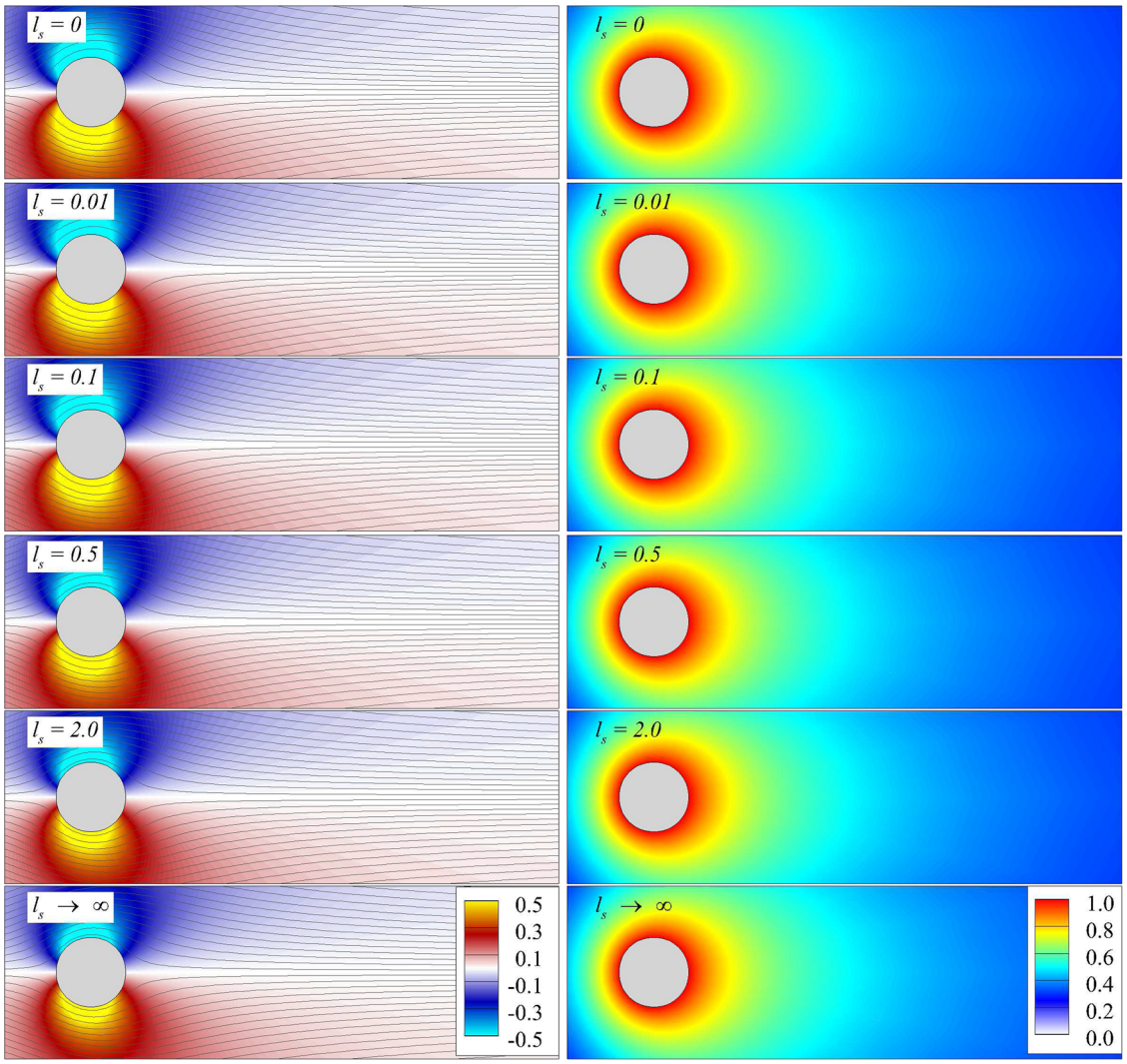

Fig. 4 (*Left*) Flow field (streamlines on top of colored vorticity contours) and (*right*) temperature distribution for $Re = 1$ and $Pr = 1$

surface to $\Theta = 0$ in the far-field, takes place over increasingly shorter distance. This contraction in the width of the transition region is indicative of a reduction in the thermal boundary layer thickness owing to the increased convective heat transfer enabled by the rising hydrodynamic slip. In the downstream region however, a reversal of this trend is observed. In this region, the area over which equispaced temperature contours are spread rises consistently with increasing hydrodynamic slip. This implies that the thermal boundary layer thickness rises with increasing slip over the downstream portion of the cylinder boundary, the rise being most prominent at the rear stagnation point. In essence, the extent of spread in isothermal contour lines clearly indicates that an increase in the hydrodynamic slip results in a decrease in the convective thermal transport in the vicinity of the rear stagnation point.

Beyond a Reynolds number of 47, the cylinder wake becomes unsteady and is characterized by the presence of von Kármán vortex street [39]. Thus, at a Reynolds number of 100, the unsteady flow separation and vortex shedding in the wake of a circular cylinder with no-slip boundary can be clearly evidenced in the top left frame of Fig. 6. An increase in l_s suppresses vorticity at the cylinder surface and reduces the unsteadiness in the wake. For $l_s \gtrapprox 0.34$, vortex shedding is eliminated completely so that steady flow fields and temperature distributions are obtained for $l_s = 0.5$, 2.0 and perfect slip cases depicted in Fig. 6. In the present case, $Pr = 1$ and $Re = 100$ so that the $Pe = 100$ is substantially higher than the two cases considered previously. The dominance of convective thermal transport is reflected in the temperature distribution depicted in the right frames of Fig. 6. Thus, variations in the temperature field remain confined to the relatively thin thermal boundary layer and the

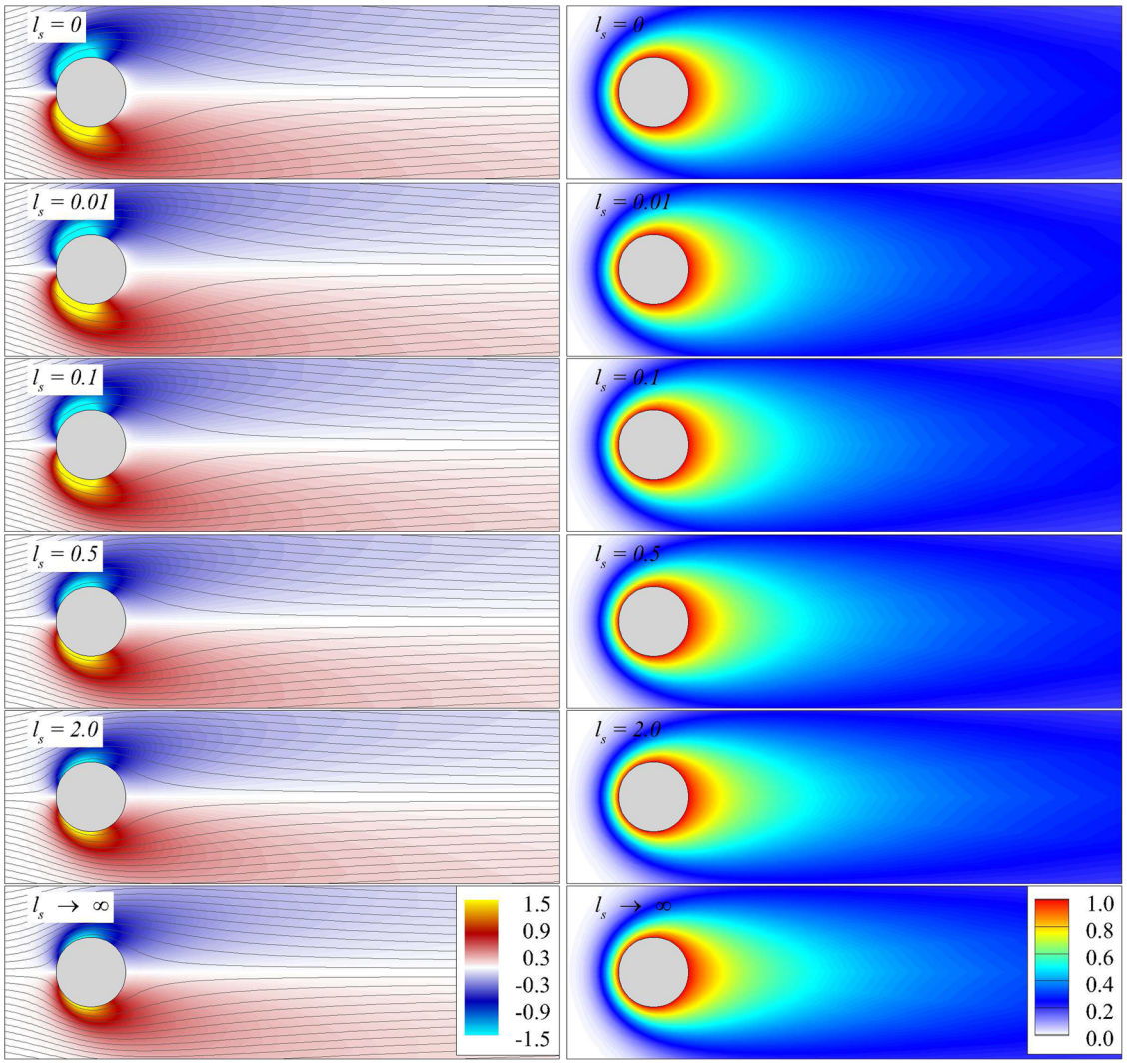

Fig. 5 (*Left*) Flow field (streamlines on top of colored vorticity contours) and (*right*) temperature distribution at $Re = 10$ and $Pr = 1$

wake regions; the extent of both of these regions reduces with an increase in hydrodynamic slip. As in the previous cases, an increase in slip leads to a discernible decrease in the thermal boundary layer thickness over the upstream portion of the cylinder. In the downstream region, especially near the wake, however, introduction of hydrodynamic slip seems to have an adverse effect on convective thermal transport. Thus, the size of the region in the wake over which temperature variations are significant increases with hydrodynamic slip and reaches a maximum for perfect slip cylinder boundary (bottom right frame of Fig. 6).

At the highest Reynolds number of 1000 investigated in this work, the observations made above are reinforced further. With an order of magnitude increase in Reynolds number, the unsteady vortex shedding from a cylinder with no-slip surface is intensified (see top left frame of Fig. 7). As in the case of $Re = 100$, hydrodynamic slip reduces vorticity at the cylinder surface and leads to eventual suppression of vortex shedding. Furthermore, when compared with the previous case of $Re = 100$ discussed above, the region over which temperature variations are discernible, diminishes much further owing to a tenfold increase in the Péclet number. As evident from Fig. 7, the regions of high thermal gradients coincide with the regions of high vorticity, namely the boundary layers on the cylinder surface, the separated shear layers, and the wake.

Even though the flow features are independent of Pr, the temperature distributions described above are strongly influenced by an increase or decrease in Prandtl number. Figure 8 depicts the temperature fields obtained from simulations for flow past a hydrodynamically slipping isothermal cylinder at a fixed Reynolds number of 100 and Prandtl numbers of 0.1 (left frames) and 10 (right frames). Among the three cases depicted

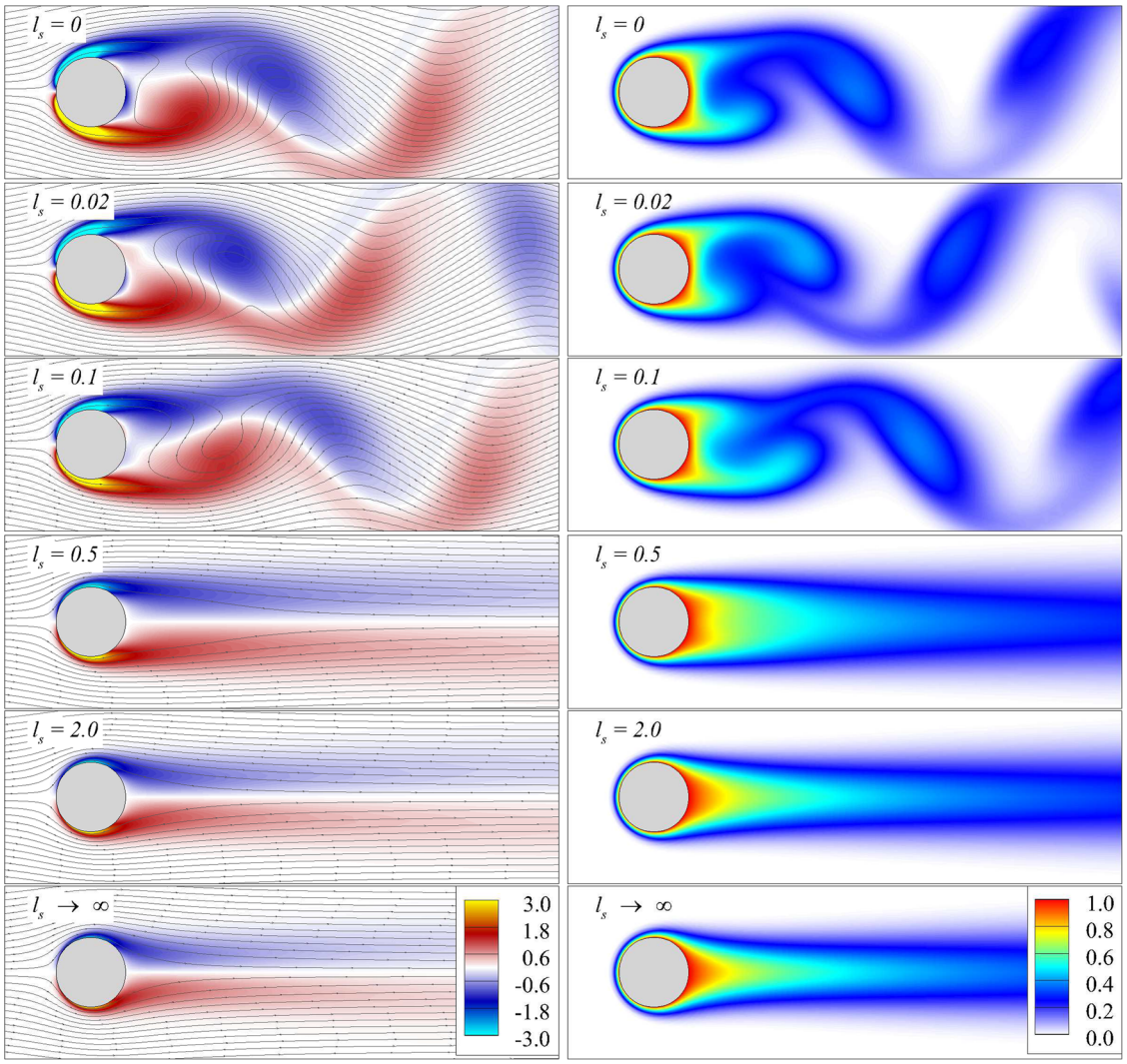

Fig. 6 (*Left*) Flow field (streamlines on top of colored vorticity contours) and (*right*) temperature distribution at $Re = 100$ and $Pr = 1$

in Fig. 8 and right frames of Fig. 6, the contribution from the diffusive thermal transport is the highest for $Pr = 0.1$ and the lowest for $Pr = 10$. Hence, at a given location in the flow field, the temperature gradients are the highest for $Pr = 10$ and the least for $Pr = 0.1$. Similar conclusions are drawn from the temperature distributions depicted in Fig. 9 at a fixed Reynolds number of 1000 and Prandtl numbers of 0.1 (left frames) and 10 (right frames). The dominance of convective thermal transport at a relatively high Péclet number of 10^4 (right frames of Fig. 9) results in a temperature distribution that resembles the dispersion of a passive tracer which simply follows the fluid particles without diffusing significantly.

The aforementioned variations in the temperature field that result from the introduction of a hydrodynamic slip influence the local Nusselt number distribution along the cylinder surface significantly. To quantify the effect of hydrodynamic slip on thermal transport from the cylinder surface, we now focus on the circumferential dependence of the local Nusselt number Nu_θ for the specific cases discussed in this section. This dependence is depicted in Figs. 10 and 11 for $Re = 1$ and 10, and, 100 and 1000, respectively, for three choices of Prandtl numbers, 0.1, 1, and 10.

At $Re = 1$ and $Pr = 0.1$, the dominance of the contribution from conduction to the net thermal transport results in a distribution of Nu_θ that is relatively insensitive to an increase in l_s. Thus, $Nu_\theta \sim \mathrm{O}(1)$ all along the cylinder surface for all slip lengths and only a slight increase (less than 2%) in the maximum local Nusselt number is observed as l_s transitions from 0 to ∞ (see top left frame of Fig. 10). An increase in Pr from 0.1 to 1 and to 10 results in an increase in both the maximum and the minimum Nu_θ at the forward and rear

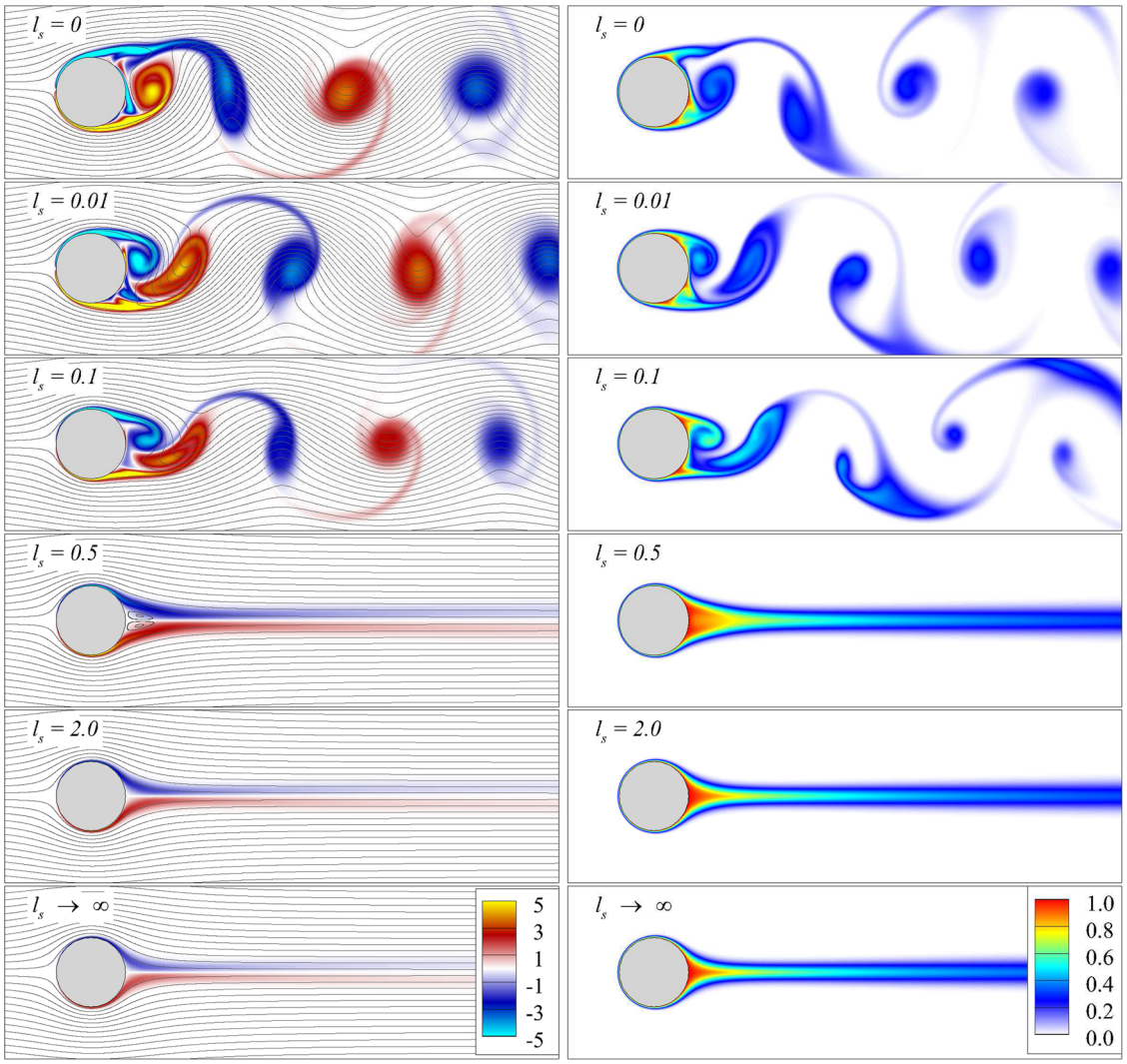

Fig. 7 (*Left*) Flow field (streamlines on top of colored vorticity contours) and (*right*) temperature distribution at $Re = 1000$ and $Pr = 1$

stagnation points, respectively (left frames of Fig. 10). The increase in the maximum Nu_θ at the forward stagnation point is most pronounced for the highest $Pr = 10$. The trends are very similar at a higher Reynolds number of 10, except that the difference between the maximum Nu_θ for the no-slip and shear-free boundaries is more pronounced (right frames of Fig. 10). At both $Re = 1$ and 10, the local Nusselt number Nu_θ decreases monotonically from a maximum at the forward stagnation point ($\theta = \pi$) to a minimum at the rear stagnation point ($\theta = 0$ or 2π) for all Pr and l_s.

With the onset of unsteady vortex shedding beyond a critical Re of 47, significant changes in the overall trends described above are observed for relatively small slip lengths ($l_s \sim \mathrm{O}(1)$), especially in the vicinity of the rear stagnation point. As shown in the top left frame of Fig. 11, at $Re = 100$ and $Pr = 0.1$, the time-averaged local Nusselt number for a no-slip cylinder surface first decreases from a maximum at the forward stagnation before increasing after reaching a minimum at the locations $\theta \approx 0.12\pi$ and 1.88π, as one traverses from upstream to downstream portion of the boundary. This non-monotonic variation in the time-averaged local Nusselt number is observed not just in the case of a no-slip but also partially slipping cylinder surface with finite l_s.

The increase in Nu_θ over the downstream portion of the cylinder surface, in the vicinity of the rear stagnation region, is appreciably higher at $Re = 100$ for $Pr = 1$ and 10 (left center and left bottom frames of Fig. 11). For $Re = 100$ and $Pr = 1$, the local maxima in Nu_θ, that is achieved at the rear stagnation point, is the highest for the no-slip surface. For a higher Pr of 10, however, the local rate of increase in Nu_θ in the

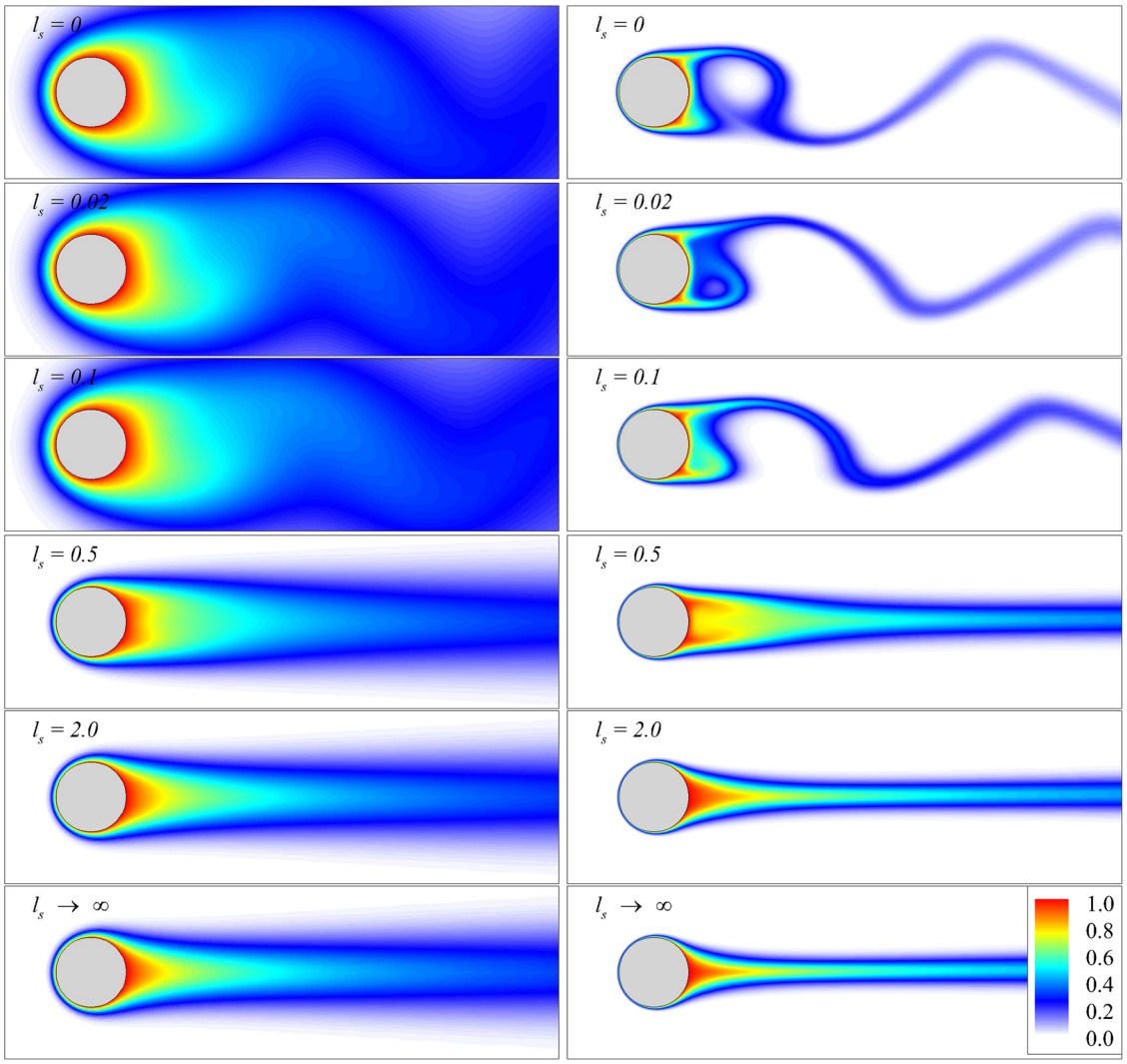

Fig. 8 Temperature distribution at $Re = 100$ for (*left*) $Pr = 0.1$ and (*right*) $Pr = 10$

vicinity of the rear stagnation region for a partially slipping surface with relatively small slip exceeds the one for a no-slip surface. Thus, at the rear stagnation point the highest Nu_θ is achieved for a partially slipping surface with $l_s \approx 0.1$. It is worth noting that for all $Pr = 0.1$, 1 and 10, for sufficiently large slip lengths ($l_s \gtrapprox 10$), the local Nu_θ exhibits a monotonic behavior in that a decrease in local Nusselt number is observed as one traverses from the forward to the rear stagnation point.

At the highest Reynolds number of 10^3, a monotonic decrease in Nu_θ from the forward to the rear stagnation point is still observed for $l_s \gtrapprox 10$ (right frames of Fig. 11). However, compared to the previous case of $Re = 100$, a stark difference in the distribution of local time-averaged Nusselt number is observed for no-slip and partially slipping surfaces with relatively small slip length. In particular, we observe strongly non-monotonic variations in the local time-averaged Nusselt number close to the rear stagnation point. For $Pr = 0.1$ and $l_s = 0$, Nu_θ rises after attaining a minima for $\theta \lessapprox 0.32\pi$ and $\theta \gtrapprox 1.68\pi$. The rate of increase declines before rising again as one approaches the rear stagnation point for a no-slip cylinder surface. For this configuration, the highest Nu_θ at the rear stagnation point is achieved for a finite slip that falls in between 0 and 0.1.

For $Re = 10^3$, $Pr = 1$ and $l_s = 0$, corresponding to a no-slip surface, an initial decrease in the Nu_θ from its global maximum at the forward stagnation point is followed by intermediate rise and decline, and an eventual increase. Thus, a total of four local maxima and minima (two each on the upper and lower halves) in Nu_θ are observed for a no-slip cylinder surface in contrast with just two in the case of $Re = 100$ and $Pr = 1$ (one each on upper and lower halves). Furthermore, at the rear stagnation point, the maximum (with respect

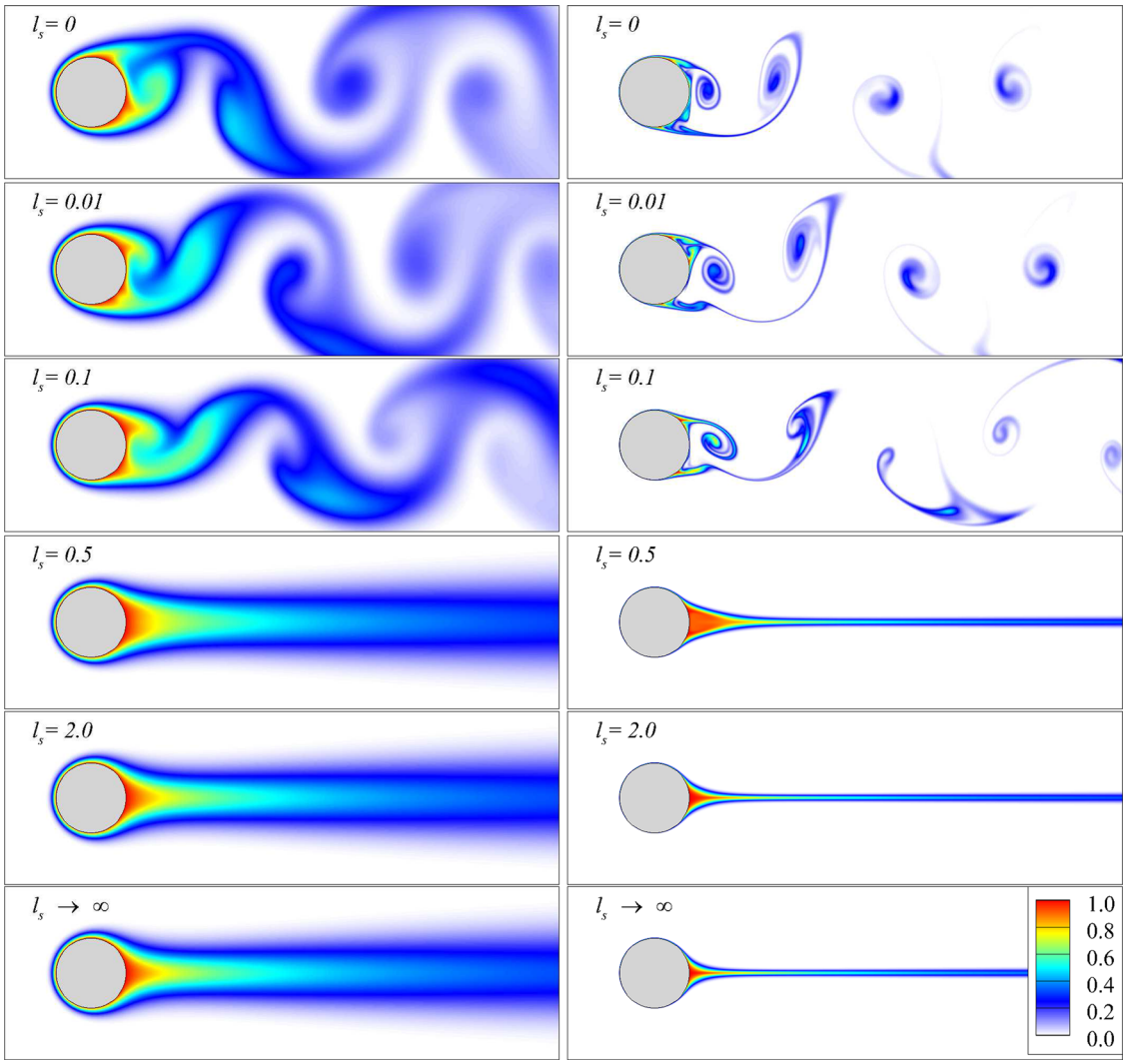

Fig. 9 Temperature distribution at $Re = 1000$ for (*left*) $Pr = 0.1$ and (*right*) $Pr = 10$

to the slip length l_s) Nusselt number of 29.5 is only slightly less than the global maximum Nu_θ of 35 for a no-slip cylinder surface. For $Pr = 10$, the non-monotonic variations in Nu_θ are significantly more prominent and as clearly evident from the bottom right frame of Fig. 11, the time-averaged local Nusselt number at the rear stagnation point for a partially slipping surface with $l_s = 0.1$ clearly exceeds the global maximum in Nu_θ (attained at the forward stagnation point) for a no-slip surface with $l_s = 0$.

The variations in the local Nusselt number distribution illustrated above clearly indicate a stark contrast in the way the hydrodynamic slip affects the convective transport from the upstream and downstream portions of the circular cylinder. Over the upstream portion, starting from the forward stagnation point to a point beyond the location at which the boundary layer separates on either side of the circular cylinder, the local Nusselt number is found to consistently increase with the hydrodynamic slip at all *Re* and *Pr*. On the contrary, in the downstream region the dependence of local Nusselt number on hydrodynamic slip is complicated by unsteady flow separation and is a strong function of both *Re* and *Pr*. In the vicinity of the rear stagnation point, hydrodynamic slip has an adverse effect on the convective transport so that the local Nusselt number in this region is the least for a shear-free boundary at all Reynolds and Prandtl numbers.

Since the non-dimensional temperature Θ is essentially a passive scalar, its distribution at high *Pe*, for prescribed *Re*, *Pr* and l_s, is determined principally by the convective transport. Therefore, one would expect that the apparent non-monotonic variation in the local Nusselt number along the downstream portion of a

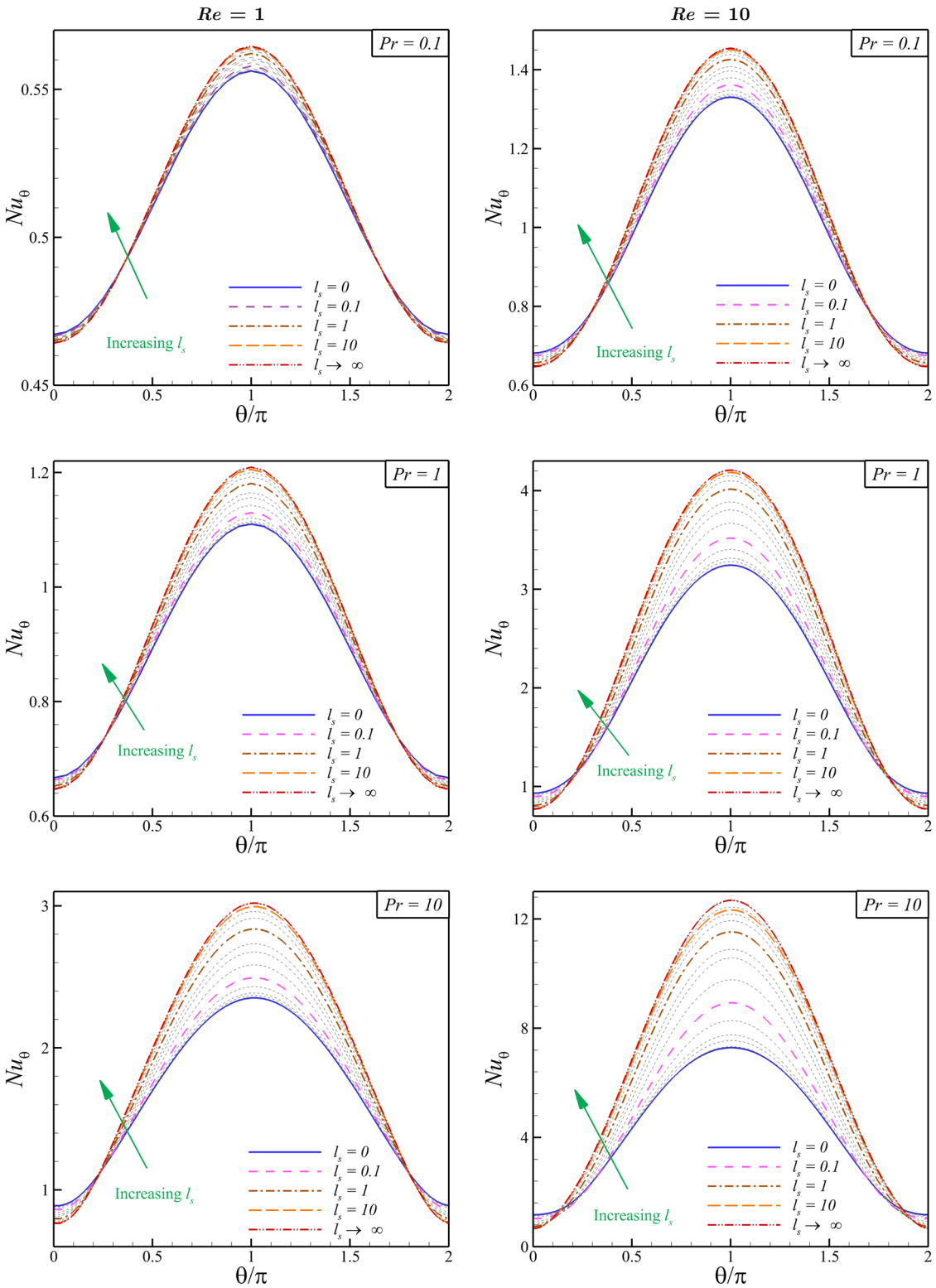

Fig. 10 Local Nusselt number Nu_θ along the cylinder surface at (*left*) $Re = 1$ and (*right*) $Re = 10$ for (*top*) $Pr = 0.1$, (*center*) $Pr = 1$ and (*bottom*) $Pr = 10$

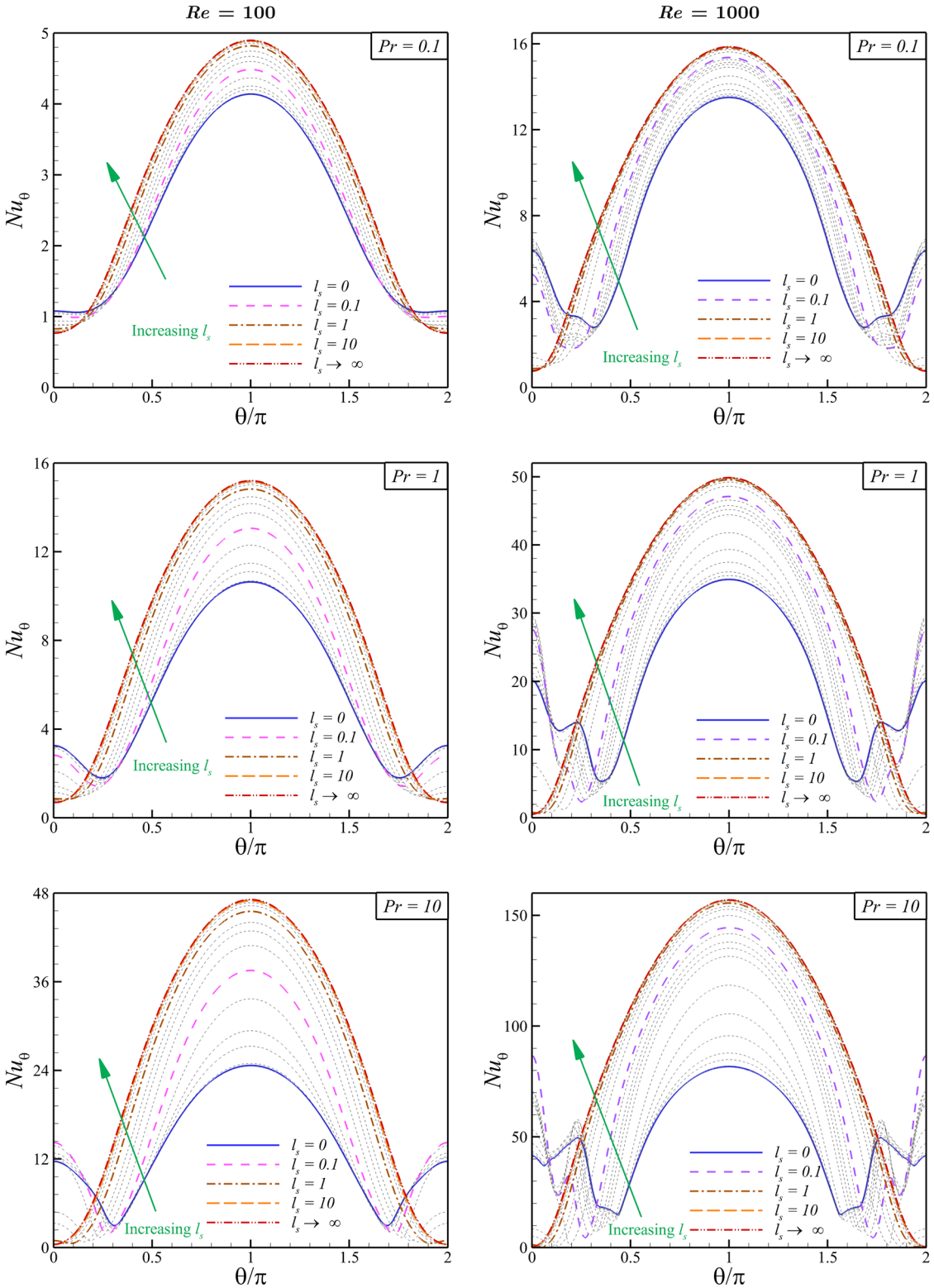

Fig. 11 Time-averaged local Nusselt number Nu_θ along the cylinder surface at (*left*) $Re = 100$ and (*right*) $Re = 1000$ for (*top*) $Pr = 0.1$, (*center*) $Pr = 1$ and (*bottom*) $Pr = 10$

hydrodynamically slipping cylinder bears a relationship with the general flow features that are observed in the vicinity of the rear stagnation point, especially at high Re and Pr.

To explore the connection between the flow field and temperature distribution, we inspect the time-averaged streamlines and radial non-dimensional temperature gradient ($a\partial\widehat{\Theta}/\partial r$) contours at $Re = 10^3$ and $Pr = 1$ for varying l_s as depicted in Fig. 12. In the case of a no-slip boundary, the time-averaged streamlines as shown in Fig. 12 indicate the existence of prominent secondary recirculating regions in addition to the primary one that is formed on the either side of the symmetry axis. The formation of such secondary pairs (referred to as the α phenomenon) is also observed during the initial stages of development in impulsively started flow past a circular cylinder at sufficiently high Reynolds number [40]. The fluid flow along the streamline joining each of the primary and secondary eddy pairs is directed toward the cylinder surface and in a small neighborhood of the cylinder boundary, closely resembles the stagnation point flow. For convenience, henceforth, we refer to this point as the secondary stagnation point, thus making it distinct from the primary forward and rear stagnation points. A strong rise in the local transport rate can therefore be expected close to each of these secondary and rear stagnation points at which the streamline joining the eddy pairs meets the cylinder surface. The time-averaged streamlines indicate a total of three such points (two secondary and one rear stagnation point) along the cylinder surface in agreement with the number of local maxima (a total of three besides the global maxima at $\theta = \pi$) that are observed in the local Nusselt number distribution at $Re = 10^3$ and $Pr = 1$ and 10 (right center and right bottom frames of Fig. 11). By symmetry the forward and rear stagnation points are both locations of maxima (global and a local maximum) in Nu_θ. The location of the second local maximum in Nu_θ ($\theta \approx 0.23\pi$) too very nearly coincides with the mean secondary stagnation point at $\theta \approx 0.25\pi$. This suggests that the local maxima in Nu_θ are indeed caused by the secondary and primary eddy pairs, with the slight difference in the mean locations most likely a result of the flow unsteadiness. The characteristic flow velocities associated with the primary and secondary eddy pairs are considerably lower than U_∞. Moreover, for the no-slip circular cylinder, the primary recirculation eddy pair is slightly displaced from the cylinder surface. These combined with the fact that the bulk temperature seen by the thermal boundary layer corresponding to the secondary eddy pair is higher than the far-field $\Theta = 0$ (see the top right frame of Fig. 7 and top frames of Fig. 9) explain why a global maximum in Nu_θ is achieved at the forward stagnation point and not at the rear or secondary stagnation points.

With rising l_s, both the strength and the size of the secondary eddy pair are diminished while those of the primary eddy enhanced progressively in the range $l_s \lessapprox 0.125$. The reduction in the strength and the size of the secondary eddy pair is accompanied by a gradual decrease in the local maximum Nu_θ at a location close to the secondary stagnation point. On the contrary, owing to a continuous increase in the size and the strength of the primary eddy pair, an enhancement in the local Nusselt number (or equivalently the time-averaged radial temperature gradient) is observed at the rear stagnation point for $l_s \lessapprox 0.125$. In effect, a substantial increase in the local Nusselt number is evidenced over both upstream and downstream portions of the circular cylinder. As a consequence, the average Nusselt number [and equivalently the normalized Nusselt number Nu_{Norm} defined by Eq. (16)] too exhibits a gradual increase for $l_s \leq 0.125$ (see Fig. 13).

For $l_s \gtrapprox 0.125$, the continued reduction in vorticity on the cylinder surface leads to a complete elimination of the secondary eddy pair and a reduction in the strength and size of the primary eddy pair. For slip lengths beyond $l_s \approx 0.125$, the radial temperature gradient at the rear stagnation point diminishes significantly as do the size and strength of the recirculating wake. The loss in overall convective transport, owing to a reduction in the radial temperature gradient in the vicinity of the rear stagnation region, overwhelms the gain from the boundary layer region so that an overall decrease in Nu is observed for $0.125 \leq l_s \leq 0.3$ for $Re = 10^3$ and $Pr > 1$ (see Fig. 13). As l_s is increased beyond 0.3, the continued gain in the local convective transport from the boundary region leads to an overall increase in the normalized Nusselt number.

At $Re = 10^3$, as evidenced from Fig. 13 and the pertinent explanation above, Nu_{Norm} exhibits a discernible non-monotonic variation with l_s. At a lower $Re = 10^2$, for intermediate slip lengths $l_s \lessapprox 0.5$, the formation of a prominent recirculating eddy pair in the wake leads to a rise in the local Nusselt number in the vicinity of the rear stagnation region (left frames of Fig. 11). However, compared to the $Re = 10^3$ case, the rise is less pronounced and the complete absence of a secondary eddy pair implies that only two local maxima, one each at the forward and rear stagnation points, are observed. More importantly, the rise in Nu_θ at the rear stagnation point is not strong enough to induce a non-monotonicity in the variation of Nu with l_s (see left frames of Fig. 14). At even lower $Re = 1$ and 10, the trends are similar in that a gradual increase in Nu_{Norm} with l_s is observed. The right frames of Fig. 14 depict the normalized maximum slip velocity as a function of l_s for $Re = 1, 10, 10^2$ and 10^3. A monotonic increase in the normalized maximum slip velocity, that is remarkably well represented by the expression Eq. (30) with appropriately chosen Re-dependent constant C,

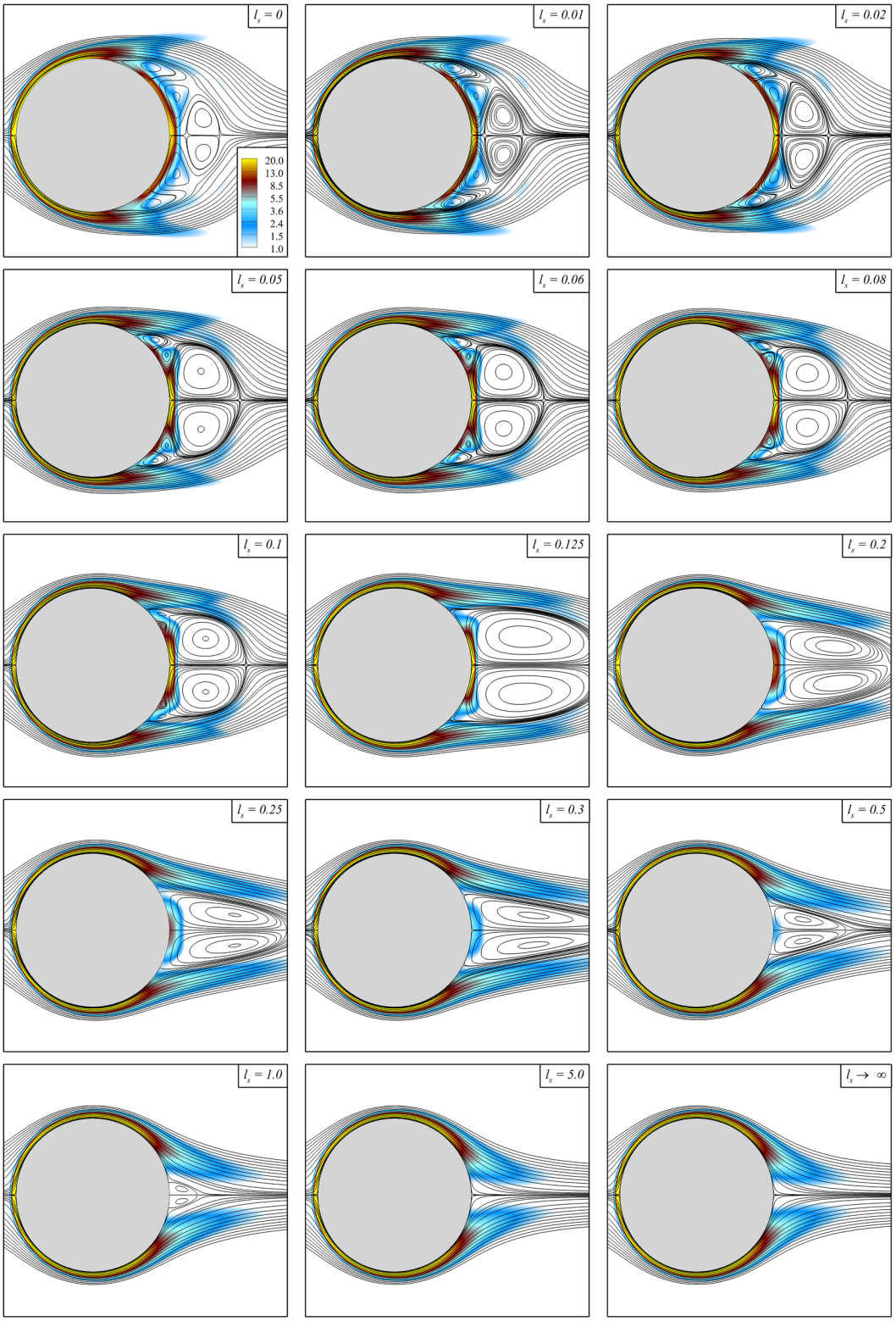

Fig. 12 Time-averaged radial temperature gradient and streamlines as a function of l_s at $Re = 10^3$ and $Pr = 1$

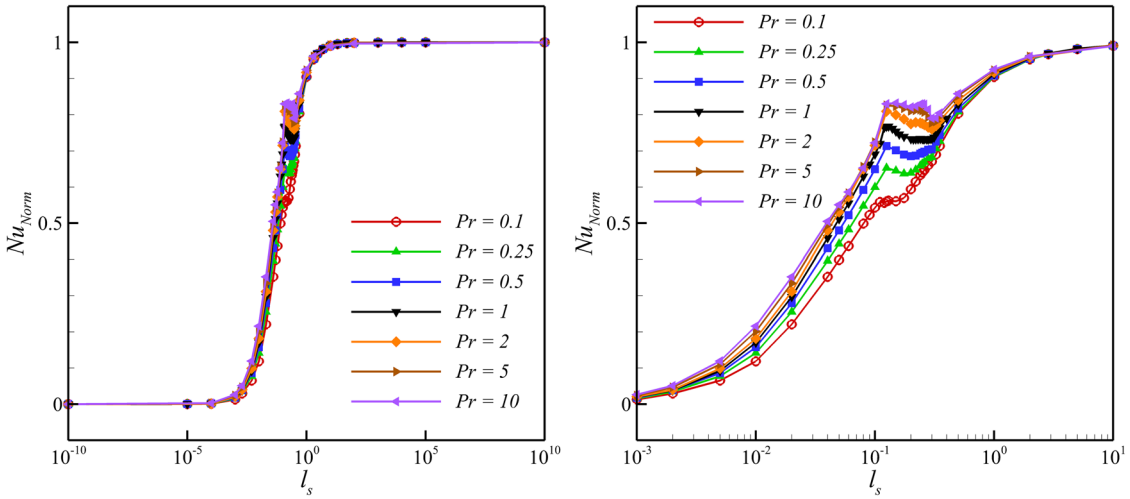

Fig. 13 Normalized Nusselt number Nu_{Norm} as a function of l_s at $Re = 1000$. Right frame depicts a close-up view of the non-monotonic transition in Nu_{Norm} with l_s

is evidenced for all Re. Moreover, as in the case of $Re \ll 1$ and $Pe \gg 1$ considered previously in Sect. 3, for $Re = 1$ and 10, the discrete data for Nu_{Norm}, as depicted in the left frames of Fig. 14, are found to be consistent with the analogous expression Eq. (17) with the Re-dependent constant C taken directly from the best fit of normalized maximum slip velocity (as shown in the right frames of Fig. 14). At higher $Re = 100$, however, the aforementioned fit exhibits considerable deviation. In this case, the distribution of the discrete data points reveals a strong dependence of Nu_{Norm} on Pr. Obviously, the expression Eq. (17) with the constant C that depends only on Re cannot account for the variations with Pr (blue colored symbols and solid line in the left frames of Fig. 14). At even higher $Re = 10^3$, the dependence of the discrete Nu_{Norm} data set on Pr is stronger. Furthermore, as discussed previously, Nu_{Norm} exhibits a non-monotonic dependence on l_s, increasing first and then decreasing before eventually rising toward the asymptotic value of 1 for all Pr. The simple expression Eq. (17) can most certainly not account for such complex variations, and therefore its comparison with the discrete data set from the simulations deteriorates considerably (brown colored symbols and solid line in the left frames of Fig. 14).

Figure 15 depicts the average Nusselt number Nu as a function of Re (left frame) and Pr (right frame) for various l_s. Nu rises with both Re and Pr with the rate of increase being higher for the shear-free surface than for a no-slip surface. For a shear-free cylinder surface, the rate of increase with respect to both Re and Pr, at sufficiently high Pe, is consistent with the scaling exponent of $1/2$ derived from the solution of thermal boundary layer equation in Sect. 3. Interestingly, the rate of increase in Nu with Re, for a partially slipping surface with $l_s = 0.1$, is discernibly higher than the rate of increase for both the shear-free and the no-slip cylinder surfaces. With increasing Reynolds number, for $l_s = 0.1$, the rise in the local Nusselt number in the vicinity of the rear stagnation far exceeds the rise over the upstream portion of the cylinder boundary. For instance, with a tenfold rise in Re from 100 to 1000, nearly six to eightfold increase in the local Nusselt number at the rear stagnation point is evidenced from Fig. 11. The corresponding three- to fourfold increase over the upstream portion is appreciably lower and consistent with the rise expected from the thermal boundary layer thinning with increasing Pe. Thus, a substantial rise in the local Nusselt number in the vicinity of the rear stagnation region, owing to an increase in the strength of the primary recirculating eddy pair, is very likely responsible for the observed steep rise in Nu with Re for $l_s = 0.1$.

5.1 Three-dimensional flow at $Re = 300$ and 1000

All our key findings in the previous sections, including the ones for $Re \geq 200$, were deduced from two-dimensional simulations. The wake of a no-slip circular cylinder is known to exhibit prominent three-dimensional features beyond $Re \approx 190$ [39,41]. For sufficiently low l_s, we can therefore expect appearance of three-dimensional instabilities in the wake corresponding to $Re \geq 200$. Moreover, it is also not immedi-

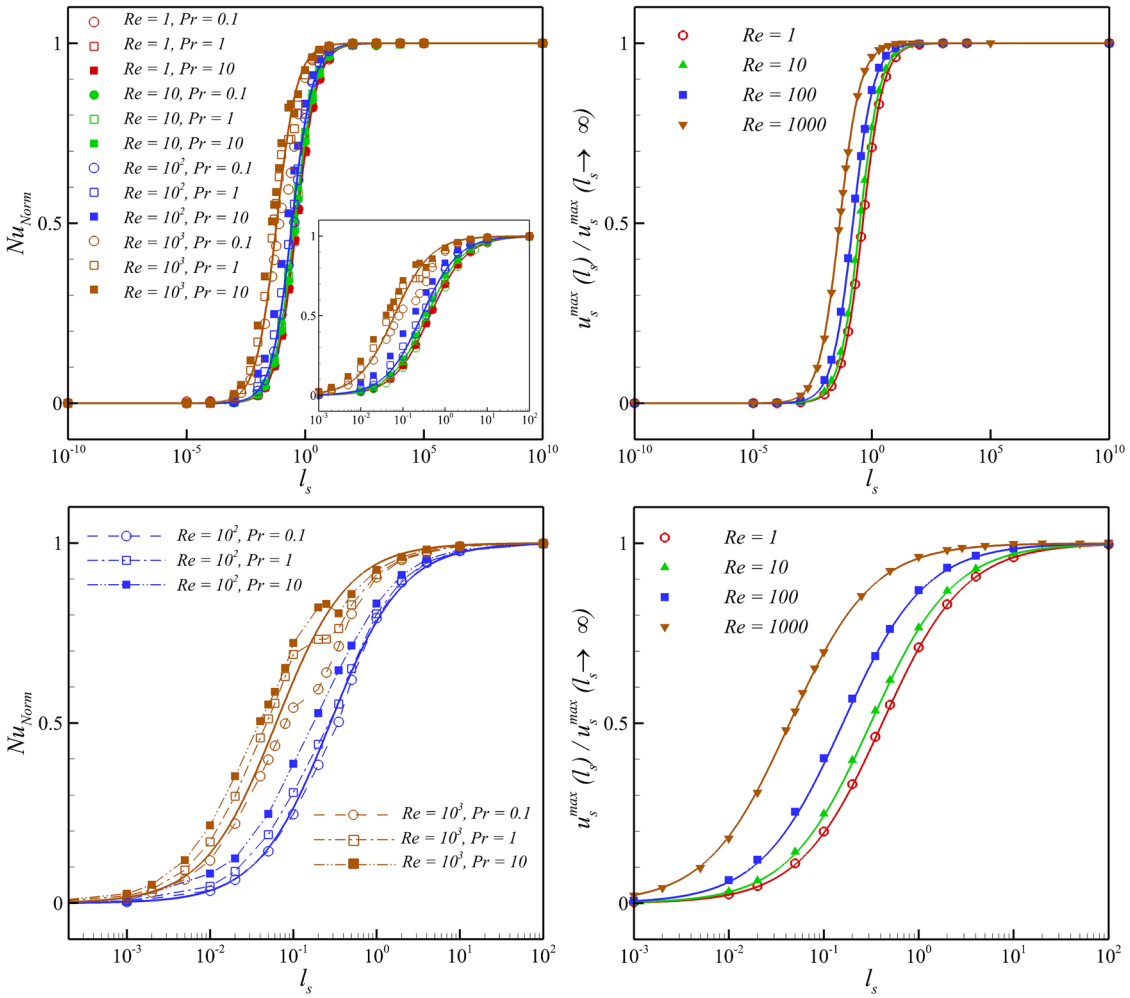

Fig. 14 Normalized (*left*) Nusselt number Nu_{Norm} and (*right*) maximum slip velocity $u_s^{\max}(l_s)/u_s^{\max}(l_s \to \infty)$ as a function of l_s for various *Re* and *Pr*. *Solid lines* in the *left* and *right* frames depict the one-dimensional curves $Nu_{\mathrm{Norm}} = l_s/(l_s + C(Re))$ and $u_s^{\max}(l_s)/u_s^{\max}(l_s \to \infty) = l_s/(l_s + C(Re))$, where for each *Re*, the constant C is determined so as to obtain the best fit to the discrete data points representing the normalized maximum slip velocity $(u_s^{\max}(l_s)/u_s^{\max}(l_s \to \infty))$ at various l_s, as computed from our simulations

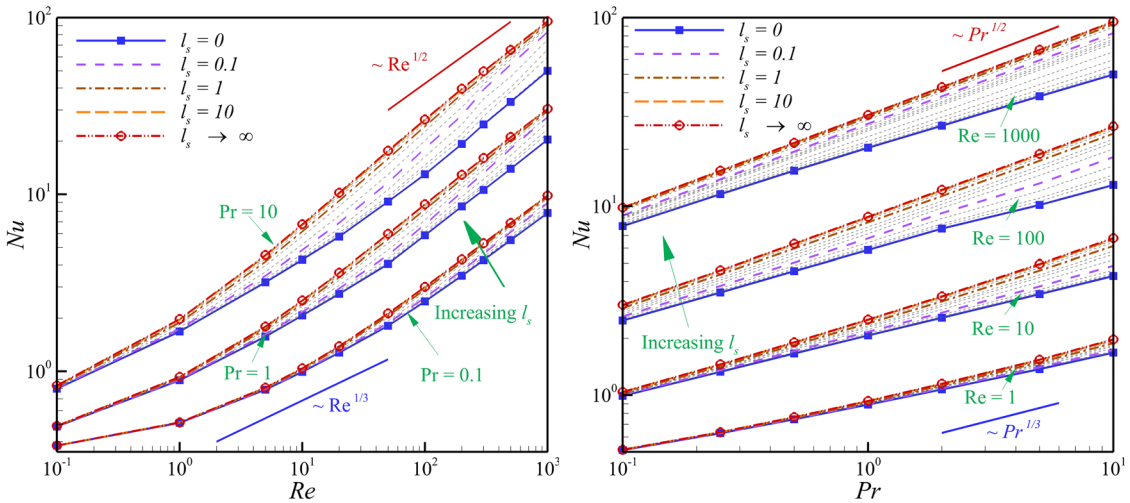

Fig. 15 Average Nusselt number Nu as a function of (*left*) *Re* and (*right*) *Pr* for various l_s

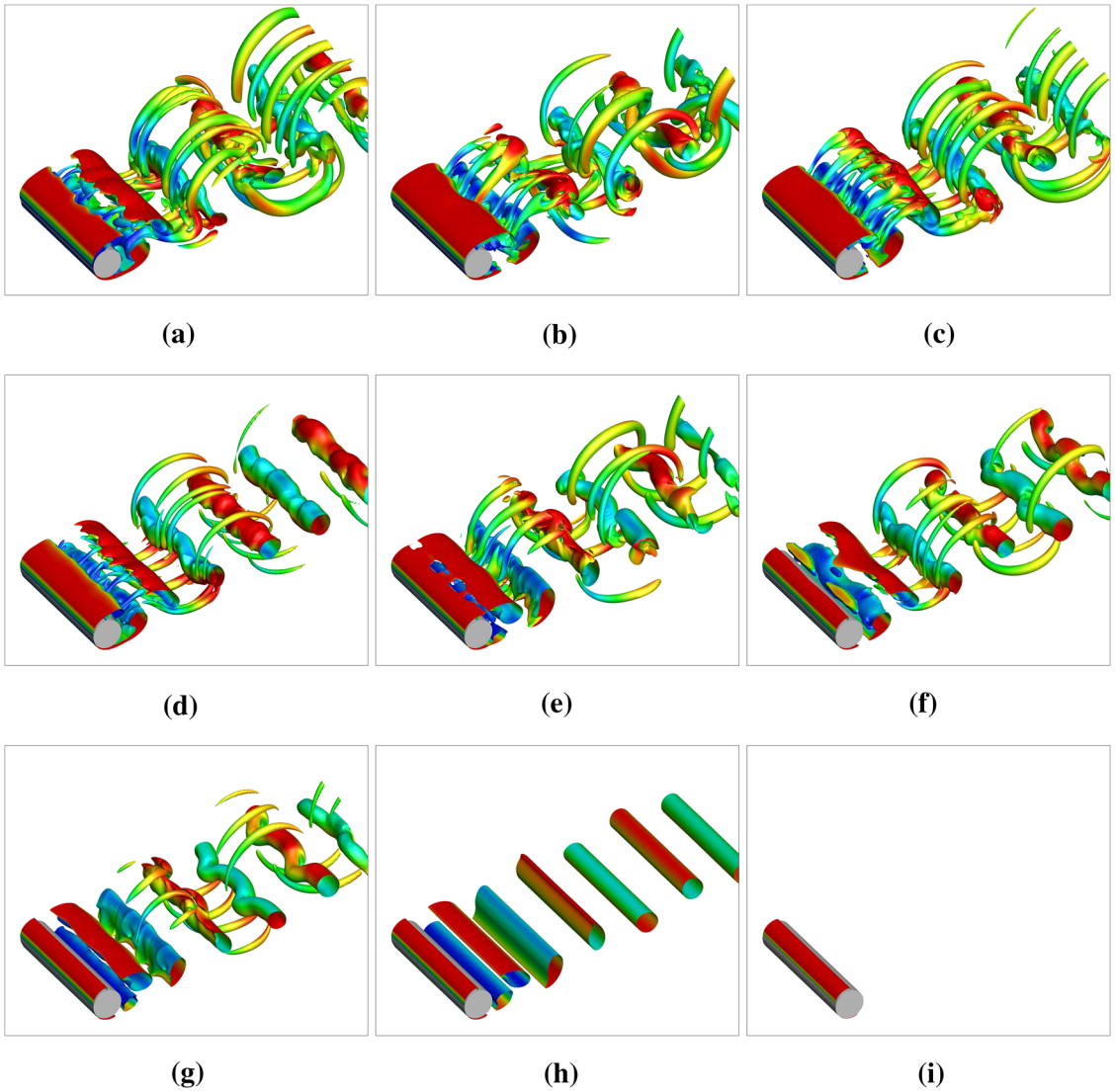

Fig. 16 Vortical structures in the wake of the cylinder at $Re = 300$ identified by $\lambda_2 = -0.1$. **a** $l_s = 0$, **b** $l_s = 0.02$, **c** $l_s = 0.04$, **d** $l_s = 0.06$, **e** $l_s = 0.08$, **f** $l_s = 0.10$, **g** $l_s = 0.12$, **h** $l_s = 0.15$, **i** $l_s = 0.5$

ately clear whether or not the three-dimensionality induced by Mode B instability beyond $Re \approx 260$ will be eliminated through introduction of a finite hydrodynamic slip on the cylinder boundary.

To establish whether or not three-dimensional wake instabilities are suppressed beyond a critical non-dimensional slip length, we perform three-dimensional simulations at $Re = 300$ and 1000 for fixed $Pr = 1$ over a range of non-dimensional slip lengths. In order to simulate flow past an infinitely long circular cylinder, we assume the spanwise direction z to be periodic with a period of $5D$. We employ a Fourier spectral discretization along the spanwise direction keeping the discretization along the radial and circumferential directions exactly the same as in two-dimensional runs of the previous section. For additional details of the generalization of our discretization methodology to three dimensions, see [31].

Figures 16 and 17 depict the instantaneous flow fields as a function of l_s for $Re = 300$ and 1000, respectively, in terms of the λ_2 isosurfaces [42] colored with the square of the magnitude of the local velocity vector ($|\mathbf{u}|^2$). For $Re = 300$, we find that the three-dimensional wake instabilities are progressively diminished with an increase in l_s. For $l_s = 0.15$, the three-dimensional instabilities are completely suppressed and the flow field attains a two-dimensional state that is characterized by the formation of classical von Kármán vortex street. For $l_s = 0.5$, the flow field is steady and free of unsteady wake vortices in agreement with the work of Legendre et al. [2]. Thus, at $Re = 300$, the critical slip length for transition from unsteady to steady wake

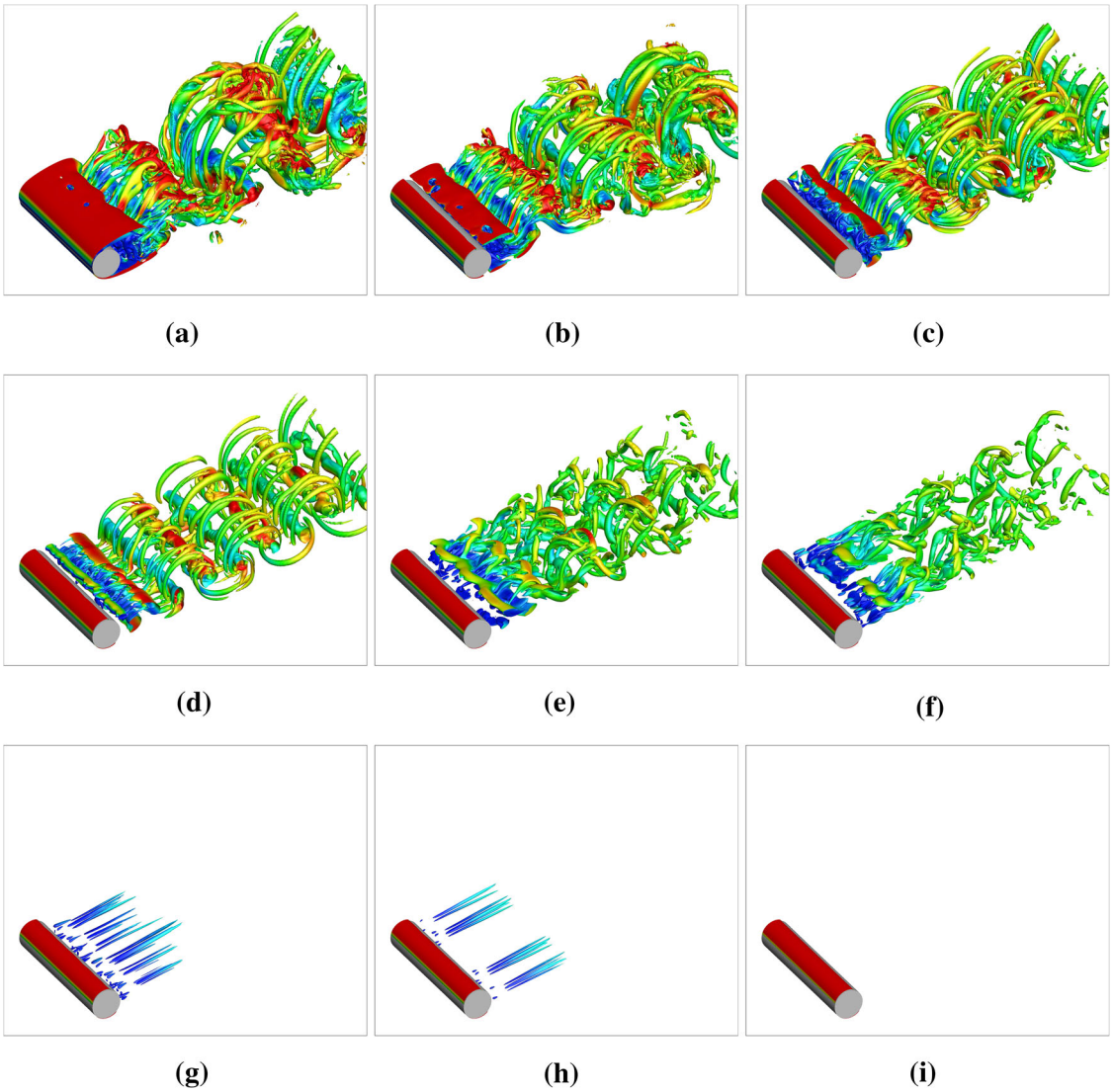

Fig. 17 Vortical structures in the wake of the cylinder at $Re = 1000$ identified by $\lambda_2 = -0.1$. **a** $l_s = 0$, **b** $l_s = 0.05$, **c** $l_s = 0.1$, **d** $l_s = 0.15$, **e** $l_s = 0.2$, **f** $l_s = 0.25$, **g** $l_s = 0.3$, **h** $l_s = 0.36$, **i** $l_s = 0.55$

exceeds the critical slip length for transition from three-dimensional to two-dimensional wake. In contrast, at a Reynolds number of 1000, we do not observe a transition from unsteady three-dimensional to an unsteady two-dimensional classical von Kármán wake and the three-dimensional features persist for relatively large non-dimensional slip lengths. Nevertheless, for sufficiently large slip lengths ($l_s = 0.55$ in Fig. 17), the three-dimensional features are completely suppressed and the flow field becomes steady and two-dimensional.

The emergence of three-dimensional wake instabilities has a significant impact on the overall convective heat transfer from the circular cylinder. Figure 18 depicts the dependence of the surface and time-averaged Nusselt number Nu on l_s for $Re = 300$ and 1000 at a fixed $Pr = 1$. The Nu computed from the three-dimensional simulation for a no-slip boundary ($l_s = 0$) is noticeably lower than the corresponding value for two-dimensional run. A reduction of the local Nusselt number in the vicinity of the rear stagnation region, owing to a lengthening of the wake vortex formation region in three dimensions, is the principal reason behind the reduced thermal transport from a cylinder with no-slip boundary. More importantly, for $Re = 1000$, a non-monotonic variation in Nu over the range $0.16 \leq l_s \leq 0.2$ is clearly evidenced from Fig. 18. Thus, as in the case of two-dimensional runs, at intermediate slip lengths, we observe a decrease in Nu with increasing l_s.

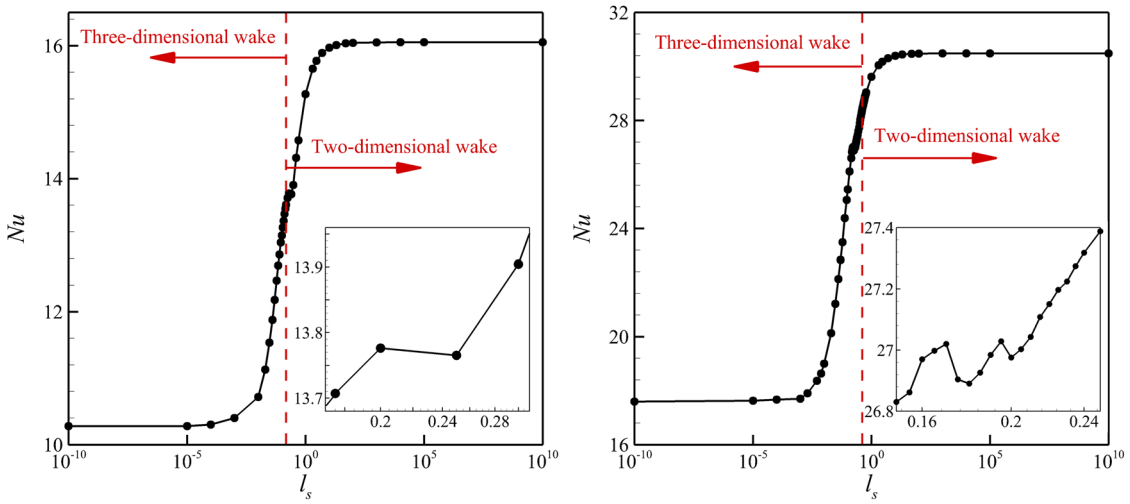

Fig. 18 Surface and time-averaged Nusselt number as a function of l_s for three-dimensional flow at (*left*) $Re = 300$ and (*right*) 1000 for $Pr = 1$

6 Conclusions

In conclusion, the effect of a prescribed hydrodynamic slip on the convective thermal transport from a heated isothermal circular cylinder placed in a uniform cross-flow of an incompressible fluid was investigated through analytical and computational techniques. For vanishingly small Re and large Pe, an explicit analytical solution of the Oseen and thermal boundary layer equations for the flow and temperature fields, respectively, led to the scaling laws $Nu \sim Pe^{1/2}$ and $Nu \sim Pe^{1/3}$ for shear-free ($l_s \to \infty$) and no-slip ($l_s = 0$) boundaries, respectively. Furthermore, for intermediate slip lengths, Nu was found to undergo a gradual transition from the lower limit for a no-slip surface to an upper limit for the shear-free boundary. The equivalence between the normalized Nusselt number Nu_{Norm} [defined in Eq. (16)] and the corresponding normalized maximum slip velocity [defined in Eq. (30)] allowed the dependence of Nu on l_s to be expressed through the simple relationship Eq. (17). For all l_s, the local Nu_θ decreased monotonically from its maximum value at the forward stagnation point to a minimum at the rear stagnation point. Moreover, the maximum Nu_θ at the forward stagnation point was found to rise monotonically from a minimum for a no-slip boundary to an asymptotic maximum for a shear-free boundary. In contrast, a complete reversal of this trend was observed at the rear stagnation point and a minimum in Nu_θ at $\theta = 0$ (the rear stagnation point) was achieved for $l_s \to \infty$.

At finite Re, results from two-dimensional simulations indicated that the overall trends described above were preserved at relatively low Re ($Re \lessapprox 25$). At higher Re, however, the formation of recirculating wake and onset of unsteady vortex shedding were found to augment local convective transport considerably. Thus, a local maximum in Nu_θ emerged at the rear stagnation point for no-slip and partially slipping boundaries with intermediate slip lengths $l_s \lessapprox \mathrm{O}(1)$. Both the wake structure, and the strength of the local maximum in Nu_θ at the rear stagnation point, were strongly influenced by Re and l_s. In particular, the formation of mean secondary eddy pairs at $Re = 10^3$ resulted in emergence of additional local maxima in the immediate neighborhood of the mean secondary stagnation points. At $Re = 10^3$, the slip length-induced variations in the size and strength of the primary recirculating eddies resulted in a pronounced rise and an eventual decline in the local Nu_θ. These variations in the local Nu_θ at $Re = 10^3$ were sufficiently strong to induce significant non-monotonicity in the otherwise monotonic dependence of the normalized Nusselt number on l_s. For sufficiently small slip lengths, the appearance of three-dimensional instabilities was found to induce significant changes in the wake structure and the surface and time-averaged Nusselt number. At a Reynolds number of 10^3, a non-monotonic dependence of Nu on l_s was evidenced over the range $0.16 \leq l_s \leq 0.2$, in three dimensions.

Our principal results, as summarized above, highlight the conflicting role of the hydrodynamic slip in increasing and decreasing convective transport from upstream and downstream portions of a circular cylinder. On the one hand, an increase in the flow velocity over the upstream portion of a hydrodynamically slipping cylinder aids convective transport from it, while on the other, the hydrodynamic slip adversely impacts convective transport by suppressing primary vortical features in the wake and is therefore a liability over the downstream portion of the cylinder. Our key observation that a strong primary recirculating region significantly

augments the local convective thermal transport is in good qualitative agreement with several prior works (see for example [43–46]) in that a marked increase in Nu_θ, owing to the presence of recirculating eddies, has indeed been observed over the downstream portion of the circular cylinder at high Re. Our results suggest that at high Re, the maximum convective transport rates will most likely be achieved for a partially slipping surface with an inhomogeneous distribution of slip length $l_s(\theta)$ that exploits the superiority of shear-free and partial slip boundary conditions over the upstream and downstream portions, respectively.

Acknowledgements The authors gratefully acknowledge support received from the Department of Science and Technology (DSTO 1329) and Supercomputing Education and Research Center-Indian Institute of Science (runtime on Cray XC40). The second author acknowledges support from the National Centre for Combustion Research and Development, Indian Institute of Science (DSTO 1086).

Appendix 1: Solution of Oseen equations for flow past a cylinder with prescribed slip

In the asymptotic limit of $Re \ll 1$, the dominance of the linear viscous terms over the inertial terms can be exploited to deduce the velocity and pressure fields for the flow past a circular cylinder with the boundary conditions (2). Note that Stokes paradox precludes the possibility of obtaining physically meaningful solutions, that satisfy the far-field and no-slip boundary conditions, using Stokes equations with complete disregard of the inertial terms. This paradox extends to the present setup for a cylinder with slip boundary condition (not shown here), and hence we consider the solution of the Oseen equations expressed in terms of the stream function ψ that satisfies the no-through-flow condition at the cylinder surface [29–31]

$$\psi = U_\infty \left(r - \frac{a^2}{r}\right) \sin\theta + \frac{U_\infty}{4} \sum_{n=1}^{\infty} \sum_{m=0}^{\infty} B_m \left\{ \left(\frac{a}{r}\right)^{n+1} \Phi_{m,n}(ka) - \Phi_{m,n}(kr) \right\} \frac{r \sin n\theta}{n}, \tag{20}$$

where

$$\begin{aligned} \Phi_{m,n}(kr) = &\{K_{m+1}(kr) + K_{m-1}(kr)\} \{I_{m-n}(kr) + I_{m+n}(kr)\} + K_m(kr) \times \\ &\times \{I_{m-n-1}(kr) + I_{m-n+1}(kr) + I_{m+n-1}(kr) + I_{m+n+1}(kr)\}, \end{aligned} \tag{21}$$

with I_p and K_q as the modified Bessel functions of pth and qth order, respectively, and $ka = Re/4$. The unknown coefficients (B_m) are determined from the slip boundary condition given on the right side of Eq. (2), and, through a standard truncation of the infinite summation in m to the leading $n-1$ terms as follows

$$B_0 = \frac{8(1+2l_s)}{\Psi_{0,1}(ka, l_s)}, \quad B_{n-1} = -\sum_{m=0}^{n-2} B_m \frac{\Psi_{m,n}(ka, l_s)}{\Psi_{n-1,n}(ka, l_s)} \quad \text{for } n > 1, \tag{22}$$

where

$$\Psi_{m,n}(ka, l_s) = (n+1)\Phi_{m,n}(ka) + ka\Phi'_{m,n}(ka) + l_s \left[(n+1)^2 \Phi_{m,n}(ka) - ka\Phi'_{m,n}(ka) - k^2a^2\Phi''_{m,n}(ka)\right]. \tag{23}$$

In the limiting case of $Re \ll 1$ (or equivalently $ka \ll 1$), the following asymptotic expressions for the modified Bessel's functions [47]

$$K_0(ka) \sim -\left\{\gamma + \ln\left(\frac{ka}{2}\right)\right\}, I_0(ka) \sim 1 \tag{24a}$$

$$K_n(ka) \sim \frac{\Gamma(n)}{2}\left(\frac{ka}{2}\right)^{-n}, I_n(ka) \sim \frac{1}{\Gamma(n+1)}\left(\frac{ka}{2}\right)^{n}, \quad n > 0, \tag{24b}$$

can be used to obtain

$$\Phi_{0,n}(ka) \sim \frac{2}{\Gamma(n+1)}\left(\frac{ka}{2}\right)^{n-1}\left[1 - n\left\{\gamma + \ln\left(\frac{ka}{2}\right)\right\}\right] \tag{25a}$$

$$\Phi_{m,n}(ka) \sim \frac{n}{2}\frac{\Gamma(m)}{\Gamma(n-m+1)}\left(\frac{ka}{2}\right)^{n-2m-1}, \quad 1 \le m \le n-1, \tag{25b}$$

and

$$\Psi_{0,n}(ka, l_s) \sim \frac{2}{\Gamma(n+1)} \left(\frac{ka}{2}\right)^{n-1} \left[n + 2nl_s(n+1) - 2n^2\,(1+2l_s)\left\{\gamma + \ln\left(\frac{ka}{2}\right)\right\}\right] \tag{26a}$$

$$\Psi_{m,n}(ka, l_s) \sim n\,\{1 + 2(m+1)l_s\}\,\frac{\Gamma(m)}{\Gamma(n-m)} \left(\frac{ka}{2}\right)^{n-2m-1}, \quad 1 \le m \le n-1, \tag{26b}$$

where $\gamma \approx 0.577$ denotes Euler's constant. Substitution of Eq. (26) in Eq. (22) yields

$$B_0 \sim \frac{4 + 8l_s}{1 - 2\gamma - 2\ln\left(\frac{ka}{2}\right) + 4l_s\left\{1 - \gamma - \ln\left(\frac{ka}{2}\right)\right\}}, \tag{27}$$

and

$$\begin{aligned} B_{n-1} \sim &- \sum_{m=1}^{n-2} \frac{1 + 2(m+1)l_s}{1 + 2nl_s} \frac{\Gamma(m)}{\Gamma(n-m)\Gamma(n-1)} \left(\frac{ka}{2}\right)^{2(n-1-m)} B_m \\ &- \frac{2\left[n + 2nl_s(n+1) - 2n^2\,(1+2l_s)\left\{\gamma + \ln\left(\frac{ka}{2}\right)\right\}\right]}{n\,(1+2nl_s)\,\Gamma(n+1)\Gamma(n-1)} \left(\frac{ka}{2}\right)^{2(n-1)} B_0 \end{aligned} \qquad \text{for } n \ge 2. \tag{28}$$

In the asymptotic limit of $ka \to 0$, only the lowest powers of ka in the above expression are of significance. Retaining only the most significant terms, it is clearly seen that for increasing index n, the coefficients B_n themselves involve increasing powers of ka so that for $ka \ll 1$ we finally deduce the following expressions for the radial and tangential components of the velocity field:

$$u_r(r,\theta) = U_\infty \cos\theta \left\{1 - \frac{a^2}{r^2} + \frac{2(1+2l_s)}{\Psi_{0,1}(ka, l_s)} \left(\frac{a^2}{r^2}\Phi_{0,1}(ka) - \Phi_{0,1}(kr)\right)\right\}, \tag{29a}$$

$$u_\theta(r,\theta) = U_\infty \sin\theta \left\{-\left(1 + \frac{a^2}{r^2}\right) + \frac{2(1+2l_s)}{\Psi_{0,1}(ka, l_s)} \left(\frac{a^2}{r^2}\Phi_{0,1}(ka) + \Phi_{0,1}(kr) + kr\Phi'_{0,1}(kr)\right)\right\}. \tag{29b}$$

For $l_s \to \infty$, above expressions reduce to the ones reported in [31] for a shear-free cylinder, while in the limit $l_s \to 0$ we recover the results of Tomotika and Aoi [29] for a cylinder with no-slip boundary condition. The following expression for the tangential surface velocity at the cylinder surface

$$u_s = u_\theta(a,\theta) = 2U_\infty \sin\theta \left\{\frac{l_s\left\{3ka\Phi'_{0,1}(ka) + k^2a^2\Phi''_{0,1}(ka)\right\}}{2\Phi_{0,1}(ka) + ka\Phi'_{0,1}(ka) + l_s\left[4\Phi_{0,1}(ka) - ka\Phi'_{0,1}(ka) - k^2a^2\Phi''_{0,1}(ka)\right]}\right\},$$

can be used to define the normalized maximum slip velocity

$$\frac{u_s^{\max}}{u_s^{\max}(l_s \to \infty)} = \frac{l_s}{l_s + C\,(Re)}, \tag{30}$$

where $u_s^{\max} = u_s(\theta = \pi/2)$ and

$$C(Re) = \frac{8\Phi_{0,1}(Re/4) + Re\Phi'_{0,1}(Re/4)}{16\Phi_{0,1}(Re/4) - Re\Phi'_{0,1}(Re/4) - Re^2/4\Phi''_{0,1}(Re/4)} \sim \frac{1}{2} - \frac{1}{4\,\{1 - \gamma - \ln(Re/8)\}}. \tag{31}$$

Appendix 2

Here, we derive a series solution to Eq. (8) and the corresponding Nusselt number with full consideration of both the linear and quadratic terms in the expansion of u_r and u_θ in Eq. (6). To begin with, we consider an expansion of the final solution for sufficiently small l_s (or equivalently α) in terms of α

$$\Theta(y,\theta,\alpha,\beta,\chi) = \Theta_0(y,\theta,\beta,\chi) + \alpha\ \Theta_1(y,\theta,\beta,\chi) + \alpha^2\ \Theta_2(y,\theta,\beta,\chi) + \cdots \tag{32}$$

where $\chi = (1 - l_s)/2$. Substituting the above expansion into Eq. (8) and then grouping terms in ascending powers of α, we obtain the following governing equations for Θ_n

$$\beta y^2 \cos\theta \frac{\partial \Theta_0}{\partial y} - \frac{\beta y \sin\theta}{\chi}\frac{\partial \Theta_0}{\partial \theta} = \frac{2}{Pe}\frac{\partial^2 \Theta_0}{\partial y^2} \tag{33}$$

and

$$\left(-\sin\theta \frac{\partial \Theta_{n-1}}{\partial \theta} + y\cos\theta \frac{\partial \Theta_{n-1}}{\partial y}\right) - \frac{\beta y \sin\theta}{\chi}\frac{\partial \Theta_n}{\partial \theta} + \beta y^2 \cos\theta \frac{\partial \Theta_n}{\partial y} = \frac{2}{Pe}\frac{\partial^2 \Theta_n}{\partial y^2} \tag{34}$$

for $n > 0$. The first term in the brackets on the left-hand side of the above equation is essentially like a source term in the above governing equation for Θ_n. Moreover, the boundary conditions for each Θ_n are given by

$$\Theta_0(y=0,\theta) = 1 \qquad \Theta_0(y\to\infty,\theta) = 0 \tag{35a}$$
$$\Theta_n(y=0,\theta) = 0 \qquad \Theta_n(y\to\infty,\theta) = 0 \qquad \text{for } n > 0. \tag{35b}$$

Next, we employ the following transformation

$$Y = \left[\left(\frac{Pe\beta}{2\chi}\right)^{\frac{1}{3}} y(\sin\theta)^{\chi}\right]^{3/2}, \qquad X = \frac{9}{4}\int_\theta^\pi (\sin\theta')^{3\chi-1}\,\mathrm{d}\theta' \tag{36}$$

to simplify the governing equation for Θ_n as follows

$$\frac{\partial \Theta_0}{\partial X} = \frac{\partial^2 \Theta_0}{\partial Y^2} + \frac{1}{3Y}\frac{\partial \Theta_0}{\partial Y} \tag{37}$$

and

$$\frac{\partial \Theta_n}{\partial X} = \frac{\partial^2 \Theta_n}{\partial Y^2} + \frac{1}{3Y}\frac{\partial \Theta_n}{\partial Y} + \Phi_n(Y,X) \tag{38}$$

for $n > 0$ where

$$\Phi_n(Y,X) = -\frac{\chi}{\beta y(Y,X)}\left[\frac{\partial \Theta_{n-1}}{\partial X} + \frac{2Y(1-\chi)\cos\theta(X)\,(\sin\theta(X))^{-3\chi}}{3}\frac{\partial \Theta_{n-1}}{\partial Y}\right] \tag{39}$$

In the transformed coordinates, the boundary conditions assume the following form

$$\Theta_0(Y=0,X) = 1 \qquad \Theta_0(Y\to\infty,X) = 0 \tag{40a}$$
$$\Theta_n(Y=0,X) = 0 \qquad \Theta_n(Y\to\infty,X) = 0 \qquad \text{for } n > 0. \tag{40b}$$

Θ_0 is given by the following similarity solution (see Sect. 3.1)

$$\Theta_0 = \int_\eta^\infty \exp\left(-\frac{t^3}{9}\right)\mathrm{d}t \Big/ \int_0^\infty \exp\left(-\frac{t^3}{9}\right)\mathrm{d}t \quad \text{where } \eta = \left(\frac{3Y}{2\sqrt{X}}\right)^{2/3} \tag{41}$$

Furthermore, Θ_n is formally given by [48]

$$\Theta_n(Y,X) = \int_0^X \int_0^\infty \Phi_n(\Upsilon,\Xi) G(Y,\Upsilon,X-\Xi)\,\mathrm{d}\Upsilon\mathrm{d}\Xi \tag{42}$$

where

$$G(Y,\Upsilon,X)=\frac{Y^{1/3}\Upsilon^{2/3}}{2X}\exp\left(-\frac{Y^2+\Upsilon^2}{4X}\right)\mathrm{I}_{1/3}\left(\frac{Y\Upsilon}{2X}\right) \tag{43}$$

In above expression, $\mathrm{I}_{1/3}$ is the modified Bessel function of the first kind [47] and $\Theta_n(Y,X)$ turns out to be nonzero only because of the finite source term in the governing equation Eq. (38). We can also represent $\Theta_n(Y,X)$ in terms of the known Θ_0 only as

$$\Theta_n(Y,X)=\left(\int_0^X\int_0^\infty D_{\Upsilon,\Xi}[\ \ ]\ G(Y,\Upsilon,X-\Xi)\,\mathrm{d}\Upsilon\mathrm{d}\Xi\right)^n\Theta_0(\Upsilon,\Xi) \tag{44}$$

where

$$\begin{aligned}D_{Y,X}[\ \ ]&=-\frac{\chi}{\beta y(Y,X)}\left(\frac{\partial[\ \ ]}{\partial X}+\frac{2Y(-\chi+1)\cos\theta(X)(\sin\theta(X))^{-3\chi}}{3}\frac{\partial[\ \ ]}{\partial Y}\right)\\&=-\left(\frac{Pe\chi^2}{2\beta^2}\right)^{1/3}\frac{(\sin\theta(X))^\chi}{Y^{2/3}}\left(\frac{\partial[\ \ ]}{\partial X}+\frac{2Y(-\chi+1)\cos\theta(X)(\sin\theta(X))^{-3\chi}}{3}\frac{\partial[\ \ ]}{\partial Y}\right)\\&=\left(\frac{Pe\chi^2}{2\beta^2}\right)^{1/3}\left(\frac{A(X)}{Y^{2/3}}\frac{\partial[\ \ ]}{\partial X}+Y^{1/3}B(X)\frac{\partial[\ \ ]}{\partial Y}\right)\end{aligned} \tag{45}$$

with

$$A(X)=-(\sin\theta(X))^\chi\qquad\text{and}\qquad B(X)=-\frac{2(-\chi+1)\cos\theta(X)(\sin\theta(X))^{-2\chi}}{3} \tag{46}$$

Next, we derive an expression for the temperature gradient at the cylinder surface $y=0$. We have

$$\left.\frac{\partial\Theta}{\partial y}\right|_{y=0}=\left.\left(\frac{\partial T}{\partial Y}\frac{\partial Y}{\partial y}\right)\right|_{Y=0}=\frac{3}{2}\left[\frac{Y\beta Pe}{2\chi}\right]^{1/3}(\sin\theta(X))^\chi\left.\left(\frac{\partial\Theta_0}{\partial Y}+\alpha\frac{\partial\Theta_1}{\partial Y}+\cdots\right)\right|_{Y=0} \tag{47}$$

We next calculate each of the terms in the expansion on the right-hand side of the above equation. Using the relationships Eqs. (41) and (44), we obtain

$$\begin{aligned}\left.\frac{\partial\Theta}{\partial y}\right|_{y=0}&=-\frac{3}{2\Gamma(\frac{1}{3})}\left(\frac{Pe\beta}{\chi X}\right)^{1/3}(\sin\theta(X))^\chi+\frac{3}{2}\alpha(\sin\theta(X))^\chi\left(\frac{Pe^2\chi}{4\beta}\right)^{1/3}\\&\quad\times\left(\frac{1}{2^{1/3}\Gamma^2(\frac{1}{3})X}\int_0^X\frac{A(\Xi)}{(X\Xi-\Xi^2)^{1/3}}\,\mathrm{d}\Xi-\frac{2^{2/3}}{\Gamma^2(\frac{1}{3})X}\int_0^X\frac{B(\Xi)\ \Xi^{2/3}}{(X-\Xi)^{1/3}}\,\mathrm{d}\Xi\right)\end{aligned} \tag{48}$$

Utilizing the above expression and the fact that for $l_s\ll 1$ or equivalently $\alpha\ll 1$ (which is the case when $\alpha\sim Pe^{-1/3}$), $\chi\approx-0.5$ and $\beta\approx\lambda/2$, we eventually arrive at the relationship Eq. (15).

References

1. Leal, L.G.: Vorticity transport and wake structure for bluff bodies at finite Reynolds number. Phys. Fluids **1**, 124–131 (1989)
2. Legendre, D., Lauga, E., Magnaudet, J.: Influence of slip on the dynamics of two-dimensional wakes. J. Fluid Mech. **633**, 437–447 (2009)
3. You, D., Moin, P.: Effects of hydrophobic surfaces on the drag and lift of a circular cylinder. Phys. Fluids **19**(8), 081701 (2007)
4. Seo, W., Song, C.G.: Numerical simulation of laminar flow past a circular cylinder with slip conditions. Int. J. Numer. Meth. Fluids **68**(12), 1538–1560 (2012)
5. Li, D., Li, S., Xue, Y., Yang, Y., Su, W., Xia, Z., Shi, Y., Lin, H., Duan, H.: The effect of slip distribution on flow past a circular cylinder. J. Fluids Struct. **51**, 211–224 (2014)
6. Rothstein, J.P.: Slip on superhydrophobic surfaces. Annu. Rev. Fluid Mech. **42**, 89–109 (2010)
7. Muralidhar, P., Ferrer, N., Daniello, R., Rothstein, J.P.: Influence of slip on the flow past superhydrophobic circular cylinders. J. Fluid Mech. **680**, 459–476 (2011)
8. Leal, L.G.: Advanced Transport Phenomena. Cambridge University Press, Cambridge (2007)

9. Haase, A.S., Chapman, S.J., Tsai, P.A., Lohse, D., Lammertink, R.G.H.: The Graetz-Nusselt problem extended to continuum flows with finite slip. J. Fluid Mech. **764**, R3 (2015)
10. Koplik, J., Banavar, R.J.: Corner flow in the sliding plate problem. Phys. Fluids **7**(12), 3118–3125 (1995)
11. Qian, T., Wang, X.-P.: Driven cavity flow: from molecular dynamics to continuum hydrodynamics. SIAM Multiscale Model. Simul. **3**(4), 749–763 (2005)
12. Nie, X., Robbins, M.O., Chen, S.: Resolving singular forces in cavity flow: Multiscale modeling from atomic to millimeter scales. Phys. Rev. Lett. **96**, 134501 (2006)
13. Snoeijer, J.H., Andreotti, B.: Moving contact lines: scales, regimes, and dynamical transitions. Annu. Rev. Fluid Mech. **45**, 269–292 (2013)
14. Kirknis, E., Davis, S.H.: Hydrodynamic theory of liquid slippage on a solid substrate near a moving contact line. Phys. Rev. Lett. **110**, 234503 (2013)
15. Thompson, P.A., Troian, S.M.: A general boundary condition for liquid flow at solid surfaces. Nature **389**, 360–362 (1997)
16. Barrat, J.-L., Bocquet, L.: Large slip effect at a nonwetting fluid-solid interface. Phys. Rev. Lett **82**, 4671–4674 (1999)
17. Lauga, E., Brenner, M.P., Stone, H.A.: Microfluidics: the no-slip boundary condition. In: Foss, J., Tropea, C., Yarin, A.L. (eds.) Handbook of Experimental Fluid Dynamics, pp. 1219–1240. Springer, New York (2007)
18. Karniadakis, G., Beskok, A., Aluru, N.: Microflows and Nanoflows: Fundamentals and Simulation. Springer, New York (2005)
19. Eckert, E.R.G., Drake, R.M.: Analysis of Heat and Mass Transfer. McGraw-Hill, New York (1987)
20. Dongari, N., Agrawal, A., Agrawal, A.: Analytical solution of gaseous slip flow in long microchannels. Int. J. Heat Mass Transf. **50**, 3411–3421 (2007)
21. Colin, S.: Gas microflows in the slip flow regime: a critical review on convective heat transfer. ASME J. Heat Transf. **134**(2), 020908 (2012)
22. Cole, J., Roshko, A.: Heat transfer from wires at Reynolds numbers in the Oseen range. In: Proceedings of Heat Transfer and Fluid Mechanics Institute. University of California (1954)
23. Levey, H.C.: Heat transfer in slip flow at low Reynolds number. J. Fluid Mech. **6**, 385–391 (1959)
24. Hieber, C.A., Gebhart, B.: Low Reynolds number heat transfer from a circular cylinder. J. Fluid Mech. **32**, 21–28 (1968)
25. Martin, M.J., Boyd, I.D.: Momentum and heat transfer in a laminar boundary layer with slip flow. J. Thermophys. Heat Transf. **20**(4), 710–719 (2006)
26. Maghsoudi, E., Martin, M.J., Devireddy, R.: Momentum and heat transfer in laminar slip flow over a cylinder. J. Thermophys. Heat Transf. **27**(4), 607–614 (2013)
27. Cai, C.: Near-continuum gas flows over a cylinder. J. Thermophys. Heat Transf. **30**(1), 25–31 (2016)
28. Navier, C.L.M.H.: Memoire sur les lois du mouvement des fluides. Mem. Acad. R. Sci. Inst. Fr. **6**, 389–440 (1823)
29. Tomotika, S., Aoi, T.: The steady flow of viscous fluid past a sphere and circular cylinder at small Reynolds numbers. Q. J. Mech. Appl. Math. **3**, 140–161 (1950)
30. Veysey, J., Goldenfeld, N.: Simple viscous flows: from boundary layers to the renormalization group. Rev. Mod. Phys. **79**, 883–927 (2007)
31. Shukla, R.K., Arakeri, J.H.: Minimum power consumption for drag reduction on a circular cylinder by tangential surface motion. J. Fluid Mech. **715**, 597–641 (2013)
32. Moore, D.W.: The boundary layer on a spherical gas bubble. J. Fluid Mech. **16**, 161–176 (1963)
33. Magnaudet, J., Eames, I.: The motion of high-Reynolds-number bubbles in inhomogeneous flows. Annu. Rev. Fluid Mech. **32**, 659–708 (2000)
34. Schlichting, H.: Boundary Layer Theory. McGraw-Hill, New York (1960)
35. Shukla, R.K., Zhong, X.: Derivation of high-order compact finite difference schemes for nonuniform grid using polynomial interpolation. J. Comput. Phys. **204**, 404–429 (2005)
36. Shukla, R.K., Tatineni, M., Zhong, X.: Very high-order compact finite difference schemes on non-uniform grids for incompressible Navier–Stokes equations. J. Comput. Phys. **224**, 1064–1094 (2007)
37. Hugues, S., Randriamampianina, A.: An improved projection scheme applied to pseudospectral methods for the incompressible Navier–Stokes equations. Int. J Numer. Meth. Fluids **28**(3), 501–521 (1998)
38. Arakeri, J.H., Shukla, R.K.: A unified view of energetic efficiency in active drag reduction, thrust generation and self-propulsion through a loss coefficient with some applications. J. Fluids Struct. **41**, 22–32 (2013)
39. Williamson, C.H.K.: Vortex dynamics in the cylinder wake. Annu. Rev. Fluid Mech. **28**, 477–539 (1996)
40. Bouard, R., Coutanceau, M.: The early stage of development of the wake behind an impulsively started cylinder for $40 \leq Re \leq 10^4$. J. Fluid Mech. **101**, 583–607 (1980)
41. Barkley, D., Henderson, R.D.: Three-dimensional Floquet stability analysis of the wake of a circular cylinder. J. Fluid Mech. **322**, 215–241 (1996)
42. Jeong, J., Hussai, F.: On the identification of a vortex. J. Fluid Mech. **285**, 69–94 (1995)
43. Perkins, H.C., Leppert, G.: Local heat-transfer coefficients on a uniformly heated cylinder. Int. J. Heat Mass Transf. **7**, 143–158 (1964)
44. Achenbach, E.: Total and local heat transfer from a smooth circular cylinder in cross-flow at high Reynolds number. Int. J. Heat Mass Transf. **18**, 1387–1396 (1975)
45. Sanitjai, S., Goldstein, R.J.: Forced convection heat transfer from a circular cylinder in crossflow to air and liquids. Int. J. Heat Mass Transf. **47**, 4795–4805 (2004)
46. Nakamura, H., Igarashi, T.: Variation of Nusselt number with flow regimes behind a circular cylinder for Reynolds numbers from 70 to 30000. Int. J. Heat Mass Transf. **47**, 5169–5173 (2004)
47. Abramowitz, M., Stegun, I.: Handbook of mathematical functions. Dover (1968)
48. Polyanin, A.D.: Handbook of Linear Partial Differential Equations for Engineers and Scientists. Chapman and Hall, Boca Raton (2001)